



# **NAVAL POSTGRADUATE SCHOOL**

**MONTEREY, CALIFORNIA**

## **THESIS**

**WAVEFRONT CONTROL FOR SPACE TELESCOPE  
APPLICATIONS USING ADAPTIVE OPTICS**

by

Matthew R. Allen

December 2007

Thesis Advisor:  
Second Reader:

Brij Agrawal  
Jae-Jun Kim

**Approved for public release, distribution is unlimited**

THIS PAGE INTENTIONALLY LEFT BLANK

<b>REPORT DOCUMENTATION PAGE</b>			<i>Form Approved OMB No. 0704-0188</i>	
Public reporting burden for this collection of information is estimated to average 1 hour per response, including the time for reviewing instruction, searching existing data sources, gathering and maintaining the data needed, and completing and reviewing the collection of information. Send comments regarding this burden estimate or any other aspect of this collection of information, including suggestions for reducing this burden, to Washington headquarters Services, Directorate for Information Operations and Reports, 1215 Jefferson Davis Highway, Suite 1204, Arlington, VA 22202-4302, and to the Office of Management and Budget, Paperwork Reduction Project (0704-0188) Washington DC 20503.				
<b>1. AGENCY USE ONLY (Leave blank)</b>		<b>2. REPORT DATE</b> December 2007	<b>3. REPORT TYPE AND DATES COVERED</b> Engineer's Thesis	
<b>4. TITLE AND SUBTITLE</b> Wavefront Control for Space Telescope Applications Using Adaptive Optics			<b>5. FUNDING NUMBERS</b>	
<b>6. AUTHOR(S)</b> Matthew R. Allen				
<b>7. PERFORMING ORGANIZATION NAME(S) AND ADDRESS(ES)</b> Naval Postgraduate School Monterey, CA 93943-5000			<b>8. PERFORMING ORGANIZATION REPORT NUMBER</b>	
<b>9. SPONSORING /MONITORING AGENCY NAME(S) AND ADDRESS(ES)</b> N/A			<b>10. SPONSORING/MONITORING AGENCY REPORT NUMBER</b>	
<b>11. SUPPLEMENTARY NOTES</b> The views expressed in this thesis are those of the author and do not reflect the official policy or position of the Department of Defense or the U.S. Government.				
<b>12a. DISTRIBUTION / AVAILABILITY STATEMENT</b> Approved for public release, distribution is unlimited			<b>12b. DISTRIBUTION CODE</b>	
<b>13. ABSTRACT (maximum 200 words)</b> <p>Future long dwell high resolution imagery satellites and space telescopes will require very large flexible primary mirrors. These large mirrors face many challenges including optical surface imperfections, structural vibrations, and jitter. A flexible mirror can overcome some of these challenges by applying adaptive optics techniques to correct mirror deformations and aberrations to produce image quality data. This paper examines and develops control techniques to control a deformable mirror subjected to a disturbance.</p> <p>The experimental portion of the work uses discrete time proportional integral control with second order filters to control disturbances in a deformable mirror and correct aberrations in an adaptive optics system using laser light. Using an adaptive optics testbed containing two deformable mirrors, two fast steering mirrors, two wave front sensors, a position sensor, and a combination of lenses the system corrects a simulated dynamic disturbance induced in the deformable mirror. Experiments using the described testbed successfully demonstrate wavefront control methods, including a combined iterative feedback and gradient control technique. This control technique results in a three fold improvement in RMS wavefront error over the individual controllers correcting from a biased mirror position. Second order discrete time notch filters are also used to remove induced low frequency actuator and sensor noise at 0.8 Hz, 2 Hz and 5 Hz. Additionally a 2 Hz structural disturbance is simulated on a Micromachined Membrane Deformable Mirror and removed using discrete time notch filters combined with a modal iterative closed loop feedback controller, showing a 36 fold improvement in RMS wavefront error over the iterative closed loop feedback alone.</p>				
<b>14. SUBJECT TERMS</b> Adaptive Optics, Beam Control, Space Telescope, Wavefront Control			<b>15. NUMBER OF PAGES</b> 109	
			<b>16. PRICE CODE</b>	
<b>17. SECURITY CLASSIFICATION OF REPORT</b> Unclassified	<b>18. SECURITY CLASSIFICATION OF THIS PAGE</b> Unclassified	<b>19. SECURITY CLASSIFICATION OF ABSTRACT</b> Unclassified	<b>20. LIMITATION OF ABSTRACT</b> UU	

NSN 7540-01-280-5500

Standard Form 298 (Rev. 2-89)  
Prescribed by ANSI Std. Z39-18

THIS PAGE INTENTIONALLY LEFT BLANK

Approved for public release, distribution is unlimited

**WAVEFRONT CONTROL FOR SPACE TELESCOPE APPLICATIONS USING  
ADAPTIVE OPTICS**

Matthew R. Allen  
Captain, United States Air Force  
B.S., Rensselaer Polytechnic Institute, 2000

Submitted in partial fulfillment of the  
requirements for the degree of

**ASTRONAUTICAL ENGINEER  
and  
MASTER OF SCIENCE IN ASTRONAUTICAL ENGINEERING**

from the

**NAVAL POSTGRADUATE SCHOOL  
December 2007**

Author: Matthew R. Allen

Approved by: Dr, Brij Agrawal  
Thesis Advisor

Dr. Jae-Jun Kim  
Co-Advisor

Anthony J. Healey  
Chairman, Department of Mechanical and Astronautical  
Engineering

THIS PAGE INTENTIONALLY LEFT BLANK

## ABSTRACT

Future long dwell high resolution imagery satellites and space telescopes will require very large flexible primary mirrors. These large mirrors face many challenges including optical surface imperfections, structural vibrations, and jitter. A flexible mirror can overcome some of these challenges by applying adaptive optics techniques to correct mirror deformations and aberrations to produce image quality data. This paper examines and develops control techniques to control a deformable mirror subjected to a disturbance.

The experimental portion of the work uses discrete time proportional integral control with second order filters to control disturbances in a deformable mirror and correct aberrations in an adaptive optics system using laser light. Using an adaptive optics testbed containing two deformable mirrors, two fast steering mirrors, two wave front sensors, a position sensor, and a combination of lenses the system corrects a simulated dynamic disturbances induced in the deformable mirror. Experiments using the described testbed successfully demonstrate wavefront control methods, including a combined iterative feedback and gradient control technique. This control technique results in a three time improvement in RMS wavefront error over the individual controllers correcting from a biased mirror position. Second order discrete time notch filters are also used to remove induced low frequency actuator and sensor noise at 0.8 Hz, 2 Hz and 5 Hz. Additionally a 2 Hz structural disturbance is simulated on a Micromachined Membrane Deformable Mirror and removed using discrete time notch filters combined with a modal iterative closed loop feedback controller, showing a 36 time improvement in RMS wavefront error over the iterative closed loop feedback alone.

THIS PAGE INTENTIONALLY LEFT BLANK



# TABLE OF CONTENTS

<b>I.</b>	<b>INTRODUCTION.....</b>	<b>1</b>
A.	MOTIVATION .....	1
B.	THESIS OBJECTIVES.....	2
C.	THESIS OVERVIEW .....	2
<b>II.</b>	<b>BACKGROUND .....</b>	<b>5</b>
A.	ADAPTIVE OPTICS.....	5
B.	ADAPTIVE OPTICS CONTROLS .....	6
<b>III.</b>	<b>EXPERIMENTAL SETUP .....</b>	<b>9</b>
A.	ADAPTIVE OPTICS TESTBED OVERVIEW.....	9
B.	DEFORMABLE MIRRORS .....	11
C.	WAVEFRONT SENSOR .....	14
D.	FAST STEERING MIRRORS .....	15
E.	POSITION SENSING MODULE .....	16
F.	LASER .....	16
G.	OPTICAL COMPONENTS.....	16
H.	SCIENCE CAMERA.....	17
I.	COMPUTER CONTROL .....	17
J.	DATA ACQUISITION.....	17
K.	CALIBRATION AND ALIGNMENT .....	18
<b>IV.</b>	<b>WAVEFRONT ESTIMATION .....</b>	<b>19</b>
A.	WAVEFRONT SENSING .....	19
1.	Shack-Hartmann Wavefront Sensor.....	19
2.	Zernike Polynomials.....	20
B.	WAVEFRONT ESTIMATION FROM WAVEFRONT SLOPE .....	23
1.	Zonal Estimation.....	23
2.	Modal Estimation.....	27
<b>V.</b>	<b>CONTROL METHODS.....</b>	<b>29</b>
A.	INFLUENCE MATRIX .....	29
B.	ITERATIVE FEEDBACK CONTROL.....	33
1.	Indirect Iterative Feedback Control .....	33
2.	Indirect Iterative Feedback Control with Singularity Robust Inverse.....	34
3.	Direct Iterative Zonal Feedback Control .....	35
4.	Direct Iterative Modal Feedback Control .....	36
C.	ITERATIVE GRADIENT FEEDBACK CONTROL .....	36
1.	Direct Gradient Approach .....	37
2.	Indirect Gradient Approach .....	40
D.	COMBINED ITERATIVE AND GRADIENT FEEDBACK .....	41
E.	FILTERING .....	41
<b>VI.</b>	<b>ANALYSIS .....</b>	<b>45</b>

A.	WAVEFRONT CORRECTION.....	45
1.	Peak to Valley Wavefront Aberation .....	45
2.	RMS Wavefront Error .....	46
B.	SURFACE CORRECTION OF THE MMDM.....	46
1.	Indirect Iterative Control.....	47
2.	Direct Iterative Control.....	49
3.	Iterative Gradient Feedback Control.....	53
4.	Combined Iterative and Gradient Feedback Control .....	56
5.	Control Method Comparison.....	58
C.	MMDM CORRECTION SUBJECT TO A DISTURBANCE .....	60
D.	NOTCH FILTERING .....	64
1.	Filtering Noisy Actuators .....	64
a.	5 Hz Sinusoidal Disturbance on Single Actuator .....	65
b.	2 Hz Sinusodial Disturbance on Single Actuator .....	66
c.	Cascaded Notch Filters on Single Actuator.....	68
d.	2 Hz and 0.8 Hz Sinusoidal Disturbance on Non-Adjacent Actuators.....	69
e.	2 Hz and 0.8 Hz Sinusoidal Disturbance on Adjacent Actuators.....	71
f.	2 Hz Sinusoidal Disturbance on 37 MMDM Actuators .....	75
2.	Filtering a Simulated Vibration.....	76
VII.	SUMMARY, CONCLUSIONS, AND FUTURE WORK.....	79
A.	SUMMARY .....	79
B.	CONCLUSION .....	79
C.	FUTURE WORK.....	80
	APPENDIX A. SOFTWARE VERSIONS.....	83
	APPENDIX B. SAMPLE MATLAB CODE .....	85
A.	INITIALIZATION .....	85
B.	WAVEFRONT SENSOR PROCESSING .....	86
C.	CONTROL ALGORITHM.....	87
	LIST OF REFERENCES .....	89
	INITIAL DISTRIBUTION LIST .....	91

## LIST OF FIGURES

Figure 1	Schematic of Typical Adaptive Optics System .....	6
Figure 2	Adaptive Optics Testbed Schematic .....	9
Figure 3	Adaptive Optics Testbed.....	10
Figure 4	Simplified MMDM Schematic (After, OKO Technologies, 2006) .....	11
Figure 5	Simplified PDM Schematic (After, OKO Technologies, 2006).....	11
Figure 6	MMDM, 15 mm, 37 Channels.....	12
Figure 7	MMDM Actuator Locations (From, OKO Technologies, 2006).....	13
Figure 8	PDM, 30 mm, 19 Channel .....	14
Figure 9	PDM Actuator Locations (From, OKO Technologies, 2006).....	14
Figure 10	Shack-Hartmann Wavefront Sensor, Basler CMOS Camera with Mask .....	15
Figure 11	Baker One Inch Fast Steering Mirror.....	15
Figure 12	Shack-Hartmann Wavefront Sensor (After, Southwell, 1980) .....	20
Figure 13	Southwell Geometry, Square Hartmann Mask (After, Southwell, 1978).....	24
Figure 14	127 Lenslet Hexagonal Hartmann Mask Used in the Adaptive Optics Testbed.....	26
Figure 15	Shack-Hartmann Lenslet 64 X-slope Response vs. MMDM Actuator 1 Control Signal (Left), Shack-Hartmann Lenslet 64 X-slope Response vs. MMDM Actuator 1 Control Signal Squared (Right).....	29
Figure 16	Shack-Hartmann Lenslet 80 X-slope Response vs. PDM Actuator 5 Control Signal .....	30
Figure 17	Iterative Feedback Control.....	33
Figure 18	Iterative Gradient Feedback Control.....	37
Figure 19	Bode Plot of Discrete Second Order Notch Filter for Different Bandwidths ..	43
Figure 20	Bode Plot of Cascaded Discrete Second Order Notch Filter for Different Bandwidths .....	44
Figure 21	Biased Wavefront of MMDM, $\sigma = 10.96$ , Peak to Valley = 17.79 waves, Control Signal Equals 240 .....	47
Figure 22	Corrected Wavefront Using Indirect Iterative Feedback Control with Shack-Hartmann Slopes and SVD Inverse, Peak to Valley = 5.42 Waves .....	48
Figure 23	Corrected Wavefront Using Indirect Iterative Feedback Control with Shack-Hartmann Slopes and Singularity Robust Inverse, Peak to Valley = 0.266 Waves.....	48
Figure 24	Error History Using Indirect Iterative Feedback Control with Shack- Hartmann Slopes with Singularity Robust Inverse and SVD Inverse .....	49
Figure 25	Corrected Wavefront Using Zonal Iterative Feedback Control, Peak to Valley = 6.0926 Waves.....	50
Figure 26	Error History Using Zonal Iterative Feedback Control .....	50
Figure 27	Corrected Wavefront Using Modal (derived from Zonal) Iterative Feedback Control, Peak to Valley = 0.268 Waves. ....	51
Figure 28	Error History Using Modal (derived from Zonal) Iterative Feedback Control .....	51

Figure 29	Corrected Wavefront Using Modal (derived from Zernike Derivatives) Iterative Feedback Control, Peak to Valley = 0.0826.....	52
Figure 30	Error History Using Modal (derived Zernike Derivatives) Iterative Feedback Control.....	53
Figure 31	Corrected Wavefront Using Iterative Gradient Feedback Minimizing Wavefront Variance, Peak to Valley = 0.735 Waves .....	54
Figure 32	Error History Using Iterative Gradient Feedback Minimizing Wavefront Variance .....	54
Figure 33	Corrected Wavefront Using Iterative Gradient Feedback Minimizing Slope Error, Peak to Valley = 0.33714 .....	55
Figure 34	Error History Using Iterative Gradient Feedback Minimizing Slope Error, 150 Iterations .....	55
Figure 35	Corrected Wavefront Using Modal (derived from Zernike Derivatives) Iterative Feedback Control, Peak to Valley = 0.0788.....	57
Figure 36	Corrected Wavefront Using Modal (derived from Zernike Derivatives) Iterative Feedback with Gradient Feedback Control, Multiple Gain, Peak to Valley = 0.0219 .....	57
Figure 37	Error History Comparing Iterative Modal Feedback and Iterative Modal Feedback Combined with Gradient Feedback .....	58
Figure 38	Multiplication Operations For Single Control Loop Iteration vs. Number of Zernike Modes Used, Using 37 Actuator Mirror, and 127 Lenslet Hartmann Mask, Modal Phase Representation from Zernike Derivatives, and Slope Representation from Measured x and y Slopes.....	59
Figure 39	RMS Wavefront Error of Planar Surface Subjected to 5 Hz Sinusoidal Disturbance with Amplitude of 54 Volts .....	61
Figure 40	Error History Using Indirect Iterative Feedback with Singularity Robust Inverse, with and without 5 Hz Sinusoidal Disturbance.....	62
Figure 41	Error History Using Direct Iterative Feedback with Modal Phase Estimation from Zernike Derivatives, with and without 5 Hz Sinusoidal Disturbance .....	62
Figure 42	Error History Using Iterative Gradient Feedback Minimizing Variance, with and without 5 Hz Disturbance .....	63
Figure 43	Error History Using Iterative Gradient Feedback Minimizing Slopes, with and without 5 Hz Disturbance.....	63
Figure 44	Error History Using Combined Direct Iterative and Gradient Feedback, with and without 5 Hz Sinusoidal Disturbance .....	64
Figure 45	Error History for 5 Hz Sinusoidal Disturbance with an Amplitude 54 Volts, on MMDM Actuator 10, with and without Notch Filter, Initial Bias of 127 .....	65
Figure 46	Control History for MMDM Actuator 10 with and without Notch Filter, 5 Hz Sinusoidal Disturbance, 54 Amplitude.....	66
Figure 47	Error History for 2 Hz Sinusoidal Disturbance with an Amplitude 54 Volts, on MMDM Actuator 10, with and without Notch Filter, Initial Bias of 127 .....	67

Figure 48	Control History for MMDM Channel 10 with and without Notch Filter, 2 Hz Sinusoidal Disturbance, 54 Amplitude.....	67
Figure 49	Error History for .08 and 2 Hz Sinusoidal Disturbance with an Amplitude 54 Volts, on MMDM Actuator 10, with and without Cascading Notch Filter, Initial Bias of 127.....	68
Figure 50	Control History for MMDM Channel 10 with and without Cascading Notch Filter, 0.8 and 2 Hz Sinusoidal Disturbance, 54 Amplitude .....	69
Figure 51	Error History for 2.0 Hz and 0.8 Hz Sinusoidal Disturbance with an Amplitude 54 Volts, on MMDM Actuator 10 and 16, with and without Notch Filter, Initial Bias of 127 .....	70
Figure 52	Control History for MMDM Channel 10 and 16 with and without Notch Filter, 2 Hz Sinusoidal Disturbance on Channel 10 and 0.8 Hz on Channel 16 with an Amplitude 54.....	70
Figure 53	Error History for 2.0 Hz Sinusoidal Disturbance with an Amplitude 54 Volts, on MMDM Actuator 10 and 11, with and without Notch Filter, Initial Bias of 127.....	71
Figure 54	Control History for MMDM Channel 10 and 11 with and without Notch Filter, 2 Hz Sinusoidal Disturbance on Channel 10 and Channel 11 with an Amplitude 54 .....	72
Figure 55	Error History for 2.0 Hz and 0.8 Hz Sinusoidal Disturbance with an Amplitude 54 Volts, on MMDM Actuator 10 and 11, with and without Notch Filter on Actuator 10, Initial Bias of 127 .....	73
Figure 56	Control History for MMDM Channel 10 and 11 with and without Notch Filter, 2 Hz and 0.8 Hz Sinusoidal Disturbance on Channel 10 and Channel 11 with an Amplitude 54 .....	73
Figure 57	Error History for 2.0 Hz and 0.8 Hz Sinusoidal Disturbance with an Amplitude 54 Volts, on MMDM Actuator 10 and 11, with and without Notch Filter, Initial Bias of 127 .....	74
Figure 58	Control History for MMDM Channel 10 and 11 with and without Notch Filter, 2 Hz Sinusoidal Disturbance on Channel 10 and 0.85 Hz on Channel 11 with an Amplitude 54 .....	75
Figure 59	Error History for 2.0 Hz Sinusoidal Disturbance with an Amplitude 54 Volts, on 37 MMDM Actuators, with and without Notch Filter, Initial Bias of 127 .....	76
Figure 60	Error History for 2.0 Hz Sinusoidal Disturbance on Wavefront Focus, with and without Notch Filter, Bandwidth = $0.2\pi$ , Initial Bias of 127 .....	77
Figure 61	Error History for 2.0 Hz Sinusoidal Disturbance on Wavefront Focus, with and without Notch Filter, Bandwidth = $0.8\pi$ , Initial Bias of 127 .....	78

THIS PAGE INTENTIONALLY LEFT BLANK

## LIST OF TABLES

Table 1	Parameters of MMDM (After, OKO Technologies, 2006).....	13
Table 2	Parameters of PDM (After, OKO Technologies, 2006) .....	14
Table 3	24 Terms of Zernike Polynomials (From, Wyant, 2003).....	22
Table 4	Experimental Condition Number of Influence Matrix for MMDM .....	32
Table 5	Error Comparison for Wavefront Control Methods.....	60
Table 6	Comparison of Control Methods Subject to a 5 Hz Sinusoidal Disturbance...	64
Table 7	Notch Filtering RMS Wavefront Error Comparison .....	78
Table 8	Software Versions.....	83

THIS PAGE INTENTIONALLY LEFT BLANK



## **ACKNOWLEDGMENTS**

I would like to express my appreciation to Distinguished Professor Brij Agrawal for allowing me to join his team and use his laboratories for my thesis research. I am grateful for his support ensuring that I had all the available tools necessary to complete my thesis. His enthusiasm to solve hard multidisciplinary problems was truly motivating.

I would like to thank Dr. Ty Martinez for his expertise in building the testbed. His hard work and patience was greatly appreciated.

I would like to give special thanks to Dr. Jae Jun Kim for an extraordinary amount of help through the thesis process. Dr. Kim provided countless hours of guidance and instruction. His personal attention kept me on track and enabled me to bring my thesis to completion.

THIS PAGE INTENTIONALLY LEFT BLANK

# **I. INTRODUCTION**

## **A. MOTIVATION**

Future space based deployable telescopes will be subject to non-atmospheric disturbances. Jitter and optical misalignment on a spacecraft can be caused by mechanical noise of the spacecraft, and settling after maneuvers. The introduction of optical misalignment and jitter can reduce the performance of an optical system resulting in pointing error and contributing to higher order aberrations. Adaptive optics such as tip/tilt fast steering mirrors can be used to control jitter in an optical system.

Large optical surfaces are also susceptible to local deviation from perfect curvature creating higher order aberrations that require corrections. Future space based optics will be made from flexible light weight materials. In an attempt to obtain a more rigid structure, smaller mirrors may also be phased together to create a larger segmented mirror. These materials and large structures will be inherently susceptible to surface errors, vibrations, and noise caused by both the environment and the spacecraft. Adaptive optics concepts and principles can correct for aberrations on the optical surface. Future space based large aperture telescopes will require robust and responsive control techniques to remove dynamic disturbances.

In order to study these problems, the Naval Postgraduate School has incorporated an adaptive optics testbed in the existing Spacecraft Research and Design Center (SRDC). This laboratory has historically studied attitude, pointing, and control methods for fine pointing of optical satellite payloads. The center has unique testbeds that simulate the spacecraft and optical systems in space like conditions. This thesis focuses on the development of adaptive optic control techniques to reduce structural disturbances in large aperture optical payloads.

## **B. THESIS OBJECTIVES**

The focus of this thesis is to investigate the adaptive optic control techniques and demonstrate them experimentally. The ultimate goal of the experimental portion is to simulate a dynamic disturbance on a deformable mirror and remove the disturbances imparted onto an incoming laser light source by removing aberrations in the wavefront using deformable mirrors and a wavefront sensor. Knowledge gained from the experimental system will be used in follow-on research using a large light weight segmented mirror.

## **C. THESIS OVERVIEW**

Chapter II provides a background on adaptive optics and adaptive optics controls. An adaptive optics system is described using a discrete time state space model.

Chapter III presents the experimental setup and the equipment used including deformable mirrors, fast steering mirrors, and sensors. The experimental layout is explained in detail.

Chapter IV discusses wavefront estimation and the principles of a Shack-Hartmann wavefront sensor. This chapter investigates wavefront reconstruction techniques that are required for wavefront control. This includes both indirect wavefront representation and direct wavefront representation using modal and zonal wavefront estimation techniques.

Chapter V discusses and compares wavefront control techniques. A traditional iterative closed loop feedback control technique is developed using both direct and indirect wavefront estimation methods. An adaptive gradient approach is discussed using modal wavefront estimation techniques. A combined iterative feedback and gradient feedback controller is also developed. Additionally a discrete time notch filter is developed to remove known disturbances from the deformable mirror surface.

Chapter VI provides experimental results and analysis of the wavefront control techniques. The control techniques are evaluated from a biased position and subject to a known low frequency disturbance.

Chapter VII provides a summary, conclusion and recommendation for future work.

THIS PAGE INTENTIONALLY LEFT BLANK

## **II. BACKGROUND**

### **A. ADAPTIVE OPTICS**

Adaptive optics is a multidisciplinary field combining expertise from physics, electro optics, controls engineering, mechanical engineering, electrical engineering, materials science and chemistry. Although many of the principles behind adaptive optics have been understood for quite some time it hasn't been until recent times that adaptive optics has become a common technology. This is primarily due to improvements in other fields including high speed computer processing, micro-electro-mechanical device technology, CMOS and CCD cameras, and improved laser systems (Tyson, 2000). The field continues to grow as more challenging applications of the field are found. A recent example is the introduction of large adaptive optics into space based telescopes like the James Webb Space Telescope. These new applications introduce new problems and challenges that can only be solved through a multidisciplinary approach.

The main purpose of an adaptive optic system is to improve the capability of an optical system by actively compensating for aberrations in real-time. An adaptive optics system can be simplified to three subsystems, Figure 1. An active mirror is the primary element where the surface can be changed to match the phase of the aberrations. Often two types of active mirrors are employed. A tip/tilt mirror is used to correct first order aberrations while a deformable mirror is used to correct for higher order aberrations. A wavefront sensor is the second element and is used to provide feedback to the active mirror in order to match the phase aberrations. A control computer is the third component combining the wavefront sensor and active mirror together by commanding the actuators of the deformable mirror.

Historically adaptive optics has been used in astronomy to remove wavefront aberrations introduced by the Earth's atmosphere, in addition to correcting the surfaces of large telescopes. Other traditional adaptive optic applications have been in beam control, particularly in the use of high energy lasers and laser communications. Improving the laser wavefront quality offers improvements for both applications of directed energy and

communications by improving the efficiency of the beam, reducing the laser power requirements (Tyson, 2000). Other applications include optical relays, both space based and airborne. In both relay applications adaptive optics are used to compensate for the distortions caused by the atmosphere.

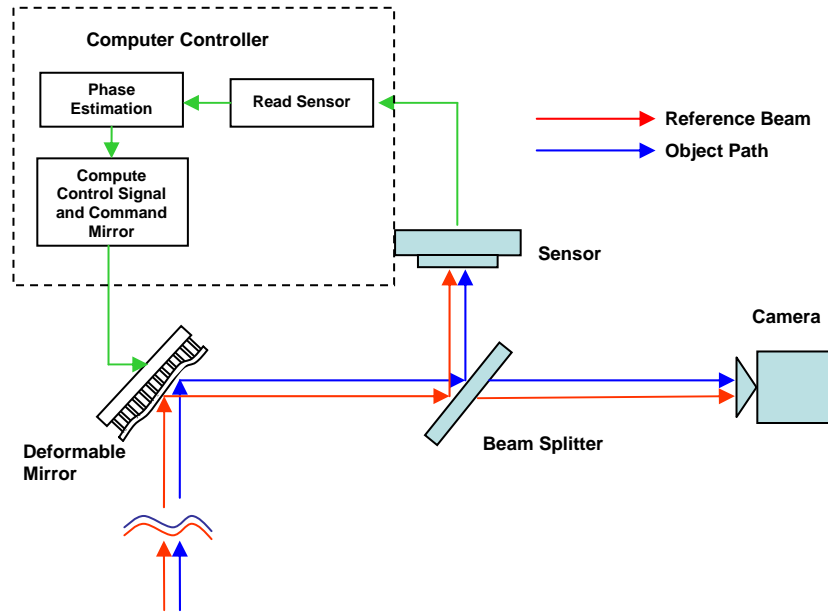


Figure 1 Schematic of Typical Adaptive Optics System

## B. ADAPTIVE OPTICS CONTROLS

In order to correct for wavefront aberrations regardless of their cause a closed loop feedback control law is required. One potential problem with wavefront control using a large mirror is control bandwidth separation from the natural frequency of the structure. The actuator control system may excite the structure while attempting to control it. An additional potential problem is the low damping of a potentially large space based mirror. This may lead to large resonant peaks in the frequency response of the structure. These responses will contribute to additional wavefront error as the surface of the mirror structure will be dynamically changing.



Adaptive optic control systems of deformable mirrors require the use of multiple control loops. The feedback from the wavefront sensor must be related to multiple actuators on the deformable mirror. What makes this control even more challenging is the fact that the individual actuator control loops are coupled. Control algorithms can be built around the discrete time state space model developed below.

An adaptive optics system can be represented by a linear state space model for the discrete time system in Equations (2.1) and (2.2), where  $x_k$  is the current state,  $u_k$  is the current control input, and  $y_k$  is the output. The matrices A, B, C, and D are the system matrices (Chen, 1993)

$$x_{k+1} = Ax_k + Bu_k \quad (2.1)$$

$$y_k = Cx_k + Du_k \quad (2.2)$$

Applying the Z-transform to the above equations and substituting  $X(z)$  into  $Y(z)$  and setting  $x(0) = 0$  results in Equation (2.6).

$$z[X(z) - x(0)] = AX(z) + BU(z) \quad (2.3)$$

$$X(z) = (zI - A)^{-1}zx(0) + (zI - A)^{-1}BU(z) \quad (2.4)$$

$$Y(z) = C(zI - A)^{-1}zx(0) + [C(zI - A)^{-1}B + D]U(z) \quad (2.5)$$

$$Y(z) = [C(zI - A)^{-1}B + D]U(z) \quad (2.6)$$

The transfer function is defined in Equation (2.7). The discrete time system is stable if every bounded input excites a bounded output sequence. The transfer function  $G(z)$  is stable if every pole of  $G(z)$  lies in the unit circle of the z-plane (Chen, 1993).

$$G(z) = \frac{Y(z)}{U(z)} = C(zI - A)^{-1}B + D \quad (2.7)$$

Applying the discrete time state space model in Equations (2.1) and (2.2) to an adaptive optics system the following model, shown in Equations (2.8) and (2.9), is developed. In this model the state vector,  $\phi$ , is the wavefront aberration, the matrix  $B$  is the influence matrix, the vector  $c$  is the vector of actuator control signals, the matrix  $\Gamma$  is a weighting matrix, the matrix  $S$  is the sensor operator, and  $y_k$  is the sensor output vector (Frazier & Tyson, 2002). The weighting matrix is a constant matrix that weighs the importance of the previous states. In the adaptive optics system used in this thesis the weighting matrix is set to an identity matrix. Therefore, no coupling or dynamics are assumed between the current state and the previous state. This assumption is appropriate as the frequency response of the deformable mirrors used is very high.

$$\phi_{x,y,k+1} = \Gamma \phi_{x,y,k} + B_{x,y} [c] \quad (2.8)$$

$$y_k = S \phi_{x,y,k} \quad (2.9)$$

The above discrete time state space model can also be used for a large mirror. However, a larger mirror will have a lower frequency response requiring the dynamics to be properly modeled. The system matrices will need to be determined experimentally or by a finite element analysis. Additional terms will also need to be added to include both the process noise and measurement noise. Despite the differences between the laboratory mirrors used in this thesis and a future large scale telescope the control law development is similar.

### III. EXPERIMENTAL SETUP

#### A. ADAPTIVE OPTICS TESTBED OVERVIEW

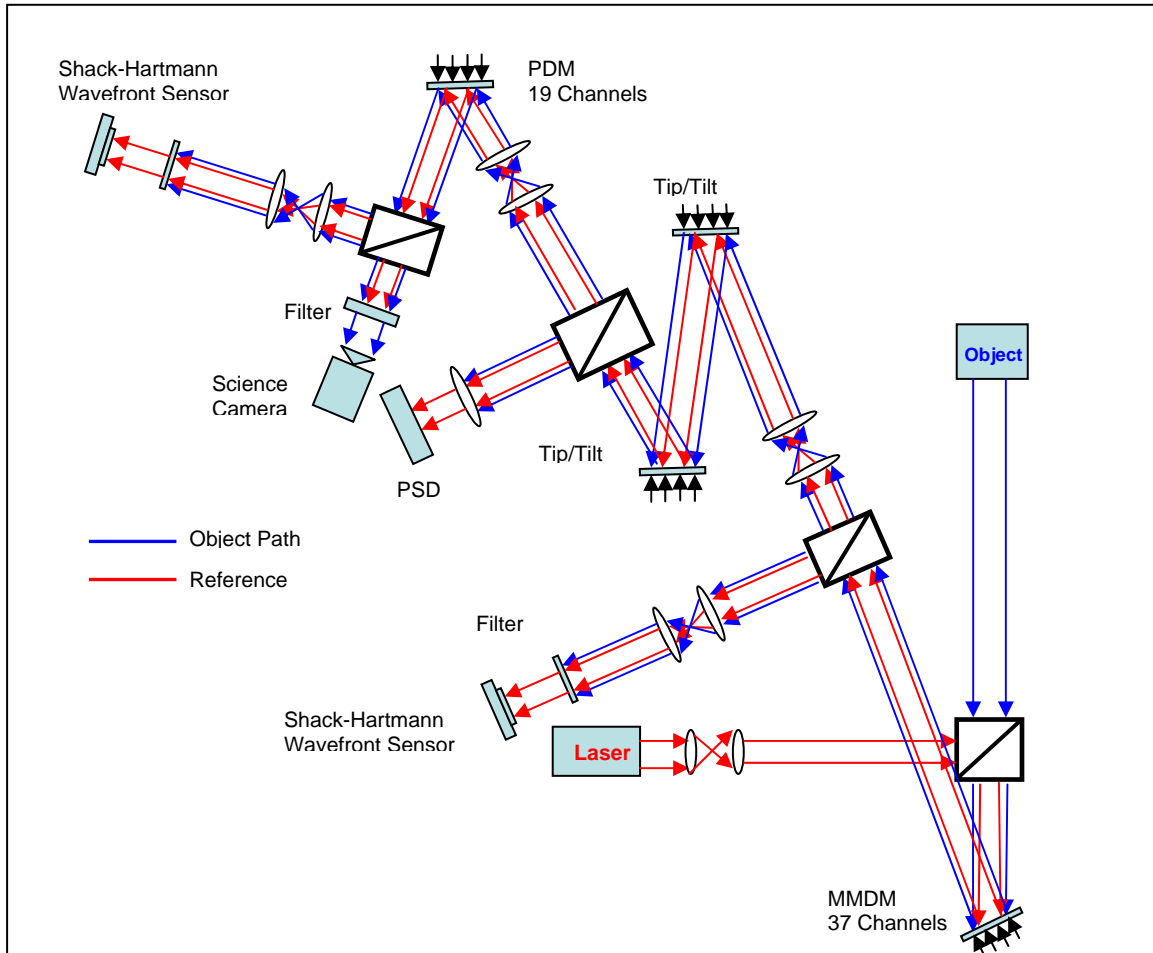


Figure 2 Adaptive Optics Testbed Schematic

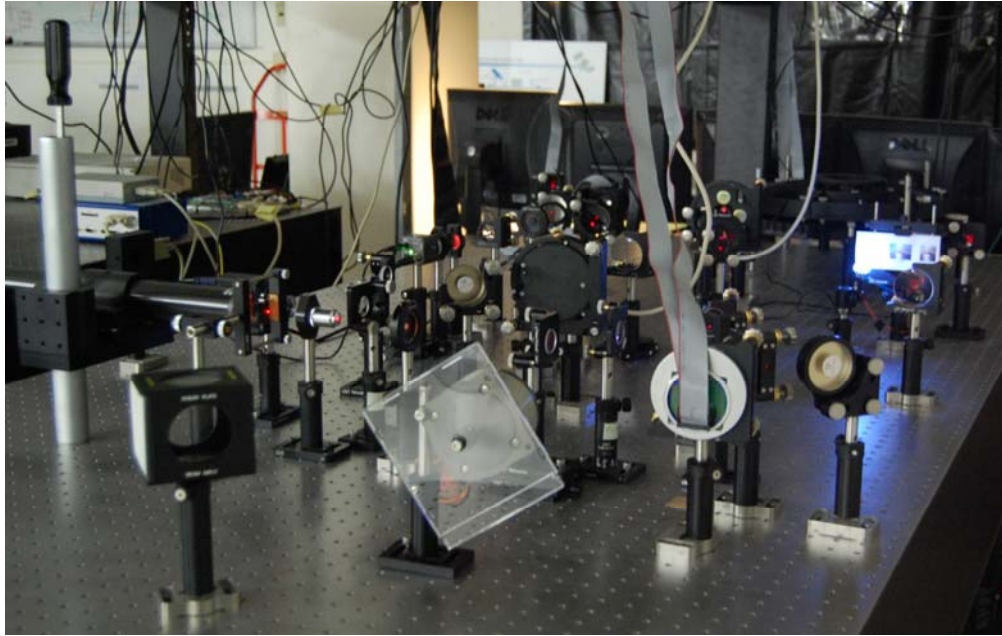


Figure 3 Adaptive Optics Testbed

The adaptive optics testbed is located in the Spacecraft Research and Design Center – Optical Relay Mirror Lab at the Naval Postgraduate School in Monterey California. The components of the testbed are mounted on a Newport Optical Bench, which can be floated to isolate the components from external vibrations. The concept is to simulate an optical satellite payload with deformable mirrors. The adaptive optics testbed uses a combination of deformable mirrors, tip/tilt fast steering mirrors, Shack-Hartmann wavefront sensors, and position sensing detectors to improve the quality of an imaged object. The light from the object of interest and a red reference laser travel together through the optical components of the testbed. Aberrations can be input into the system through additional optical components or by a deformable mirror. A Shack-Hartmann wavefront sensor samples the wavefront to provide feedback to a control algorithm which controls a deformable mirror to compensate for the aberrations.

The purpose of the testbed is to demonstrate advanced control algorithms that could be applied to an optical payload. The testbed is set up with three different control loops. The first control loop consists of a Micromachined Membrane Deformable Mirror (MMDM) and Shack-Hartmann wavefront sensor. This first loop represents a primary

deformable mirror on a space telescope. The second control loop consists of two Baker Adaptive Optics Fast Steering Mirrors (FSM) and a Position Sensing Detector (PSD). The second loop compensates for optical misalignment and controls tip/tilt aberrations attributed to jitter. The third control loop consists of a Piezoelectric Deformable Mirror (PDM) and a Shack-Hartmann wavefront sensor. The final loop is used to control higher order wavefront aberrations.

## B. DEFORMABLE MIRRORS

Two OKO Technologies deformable mirrors are used in the experimental setup, a MMDM and a PDM. The MMDM is a membrane mirror, with a 5  $\mu\text{m}$  membrane mounted over a two dimensional array of electrodes. By applying a potential between the electrodes and the membrane, the membrane shape deforms. The PDM is made from a thin solid plate of glass. The plate is bonded to a two dimensional array of piezoelectric actuators. By elongating the piezoelectric actuators the mirror deforms (OKO Technologies, 2006).

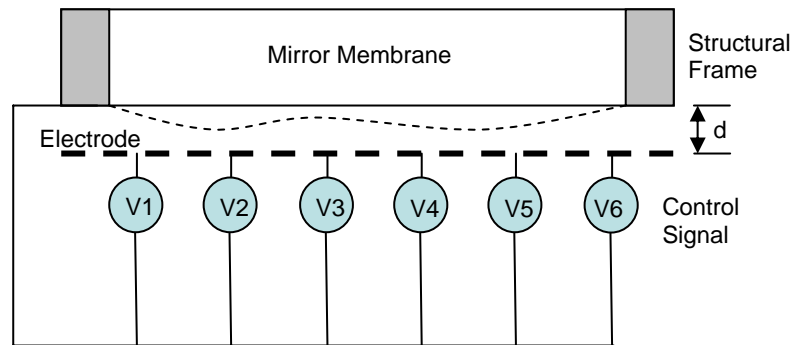


Figure 4 Simplified MMDM Schematic (After, OKO Technologies, 2006)

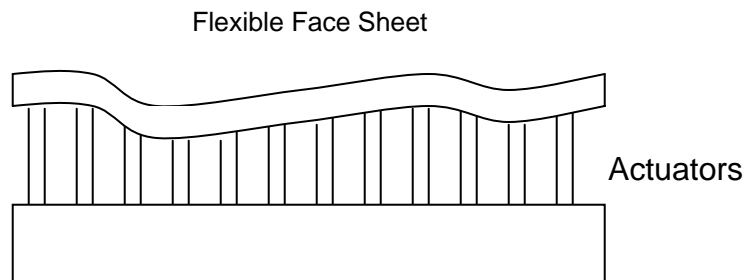


Figure 5 Simplified PDM Schematic (After, OKO Technologies, 2006)

The MMDM and PDM only actuate in one direction, from zero voltage due to electrostatic forces. Therefore, to achieve bi-directional control over the mirrors they are biased to a half way point. By biasing the mirror the actuators can push and pull from the biased position. The MMDM and PDM individual actuators are actuated by applying an 8-bit control signal between 0 and 255, which is then applied as a voltage through the mirror electronics. The MMDM surface deflection is linearly dependent on the square of the applied voltage. The control signal can also be represented as a value between +/-1. The value zero represents the biased position, the values of +/-1 represents the full positive or negative actuation. Therefore, given a value,  $c$ , between +/- 1 to a MMDM actuator, Equation (3.1) is used to compute the applied control signal. The PDM deflection is linearly dependent on the voltage, Equation (3.2). Therefore, the biased position for the MMDM is at an applied control signal of approximately 180 and the bias position for the PDM is at an applied control signal of 127.

$$V_{MMDM} = ((c + 1).5)^{1/2} (255) \quad (3.1)$$

$$V_{PDM} = ((c + 1).5)(255) \quad (3.2)$$

The MMDM used in the experimental setup is 15 mm in diameter and has 37 channels, as shown in Figure 6. The mirror is composed of a silicon chip mounted over a holder. The holder contains the electrode structure and the chip contains a silver nitride membrane, which is coated to form the mirror surface and grounded. The technical details of the mirror are provided in Table 1 and the actuator locations are shown in Figure 7. The frequency range of the mirror is between 0 and 500 Hz.

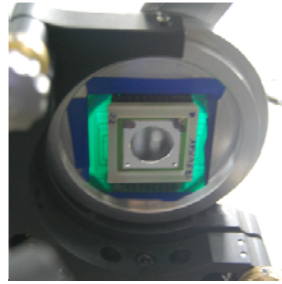


Figure 6 MMDM, 15 mm, 37 Channels

Parameter	Value
Aperture	Circular
Coating	Silver Nitride
Aperture Diameter	15 mm
Number of Electrodes	37
Control Voltage	0-300 Volts
Initial RMS Deviation From Plane	< .45 $\mu\text{m}$
Maximum Deflection at Center	10 $\mu\text{m}$

Table 1 Parameters of MMDM (After, OKO Technologies, 2006)

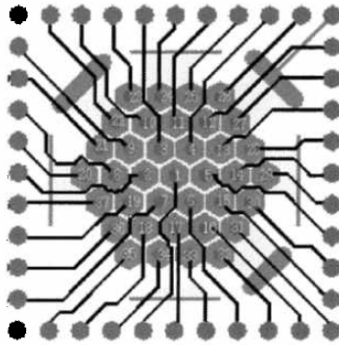


Figure 7 MMDM Actuator Locations (From, OKO Technologies, 2006)

The PDM used in the experimental setup is 30 mm in diameter and has 19 actuators, as shown in Figure 8. The reflective plate is attached to the actuator structure and coated with a mirror surface. The technical details of the mirror are shown in Table 2 and the actuator locations are shown in Figure 9. The frequency range of the mirror is between 0 and 1 kHz.



Figure 8 PDM, 30 mm, 19 Channel

Parameter	Value
Aperture	Circular
Aperture Diameter	30 mm
Number of Electrodes	19
Control Voltage	0-400 Volts
Initial RMS Deviation From Plane	$< .1 \mu\text{m}$
Maximum Deflection at Center	$8 \mu\text{m}$ at 400V

Table 2 Parameters of PDM (After, OKO Technologies, 2006)

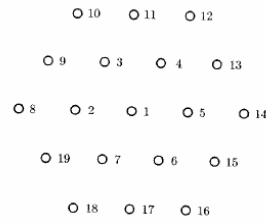


Figure 9 PDM Actuator Locations (From, OKO Technologies, 2006)

### C. WAVEFRONT SENSOR

The Shack-Hartmann wavefront sensor used in the experimental setup is an OKO Technologies Shack-Hartmann wavefront sensor. The sensor includes a  $\frac{1}{2}$ -inch Complimentary Metal-Oxide Semiconductor (CMOS) camera model A601f made by Basler, Germany. The camera has 656x491 pixels and can operate at 60 frames per second (fps) and has a clear aperture of 3.9 mm. The Hartmann mask is made of fused



silica and has a hexagonal geometry, with an aperture of 3.5 mm consisting of 127 subapertures with a diameter of 100  $\mu\text{m}$  (OKO Technologies, 2006).



Figure 10 Shack-Hartmann Wavefront Sensor, Basler CMOS Camera with Mask

#### **D. FAST STEERING MIRRORS**

The two fast steering mirrors (FSMs) were built by Baker Adaptive Optics and are shown in Figure 11. The purpose of the first FSM is to introduce disturbances and vibrations in the beam. The second FSM is then used to remove the disturbance by using feedback from the position sensing device. The FSM has a one inch diameter mirror and uses voice coils to actuate the mirror. The voice coils are placed orthogonally to drive the mirror in the X and Y directions (tip and tilt). The FSMs have a natural frequency at approximately 230 Hz depending on the direction of motion and a control of less than 350 Hz depending on direction of motion. The FSMs are controlled using MATLAB, SIMULINK and DSPACE by applying a voltage between +/-5 volts.



Figure 11 Baker One Inch Fast Steering Mirror

## **E. POSITION SENSING MODULE**

Jitter is measured using a Position Sensing Detector (PSD). This detector consists of both a position sensing module and an amplifier. The detector and amplifier are manufactured by On-Trak Photonics Inc. and are models PSM2-10 and OT-301 respectively. The position sensing module is a packaged silicon position sensing photodiode chip that produces an analog output directly proportional to the position of a light spot on the detector. The PSD measures the reference laser's position on the position sensing module. The module is a 10 mm x 10 mm duo-lateral silicon chip that can measure wavelengths between 400 and 1100 nm. The typical resolution is 250 nm and the linearity between analog output and position is within 0.3% (On-Trak Photonics Inc., 2005).

## **F. LASER**

The reference laser used is a red helium neon laser made by JDS Uniphase, model 1137P. The operating wavelength is 632.8 nm with a beam diameter of 0.81 mm. The laser has low noise with a maximum RMS of 0.2, and long term amplitude stability of 2.5% max drift over 8 hours. The beam pointing stability starting at 25°C is less than 0.10 mrad. The laser provides a collimated beam of light that is used as a reference to determine aberrations of other optical components (JDSU, 2007).

## **G. OPTICAL COMPONENTS**

Lenses are used to manage the reference beam diameter and ensure that the reference laser beam is collimated. The lenses used in the testbed setup include a 20X microscope objective, and multiple doublets of different focal lengths. A microscope objective is the first lens used as a beam expander in the optical path of the reference beam. The microscope objective in combination with a doublet lens expands the beam to a one inch beam. The doublet lenses are used to manage diameter of the beam as it travels through the testbed. A spatial filter is not used as the laser used produces a high quality beam. Beam splitters are used to divert a percentage of the reference beam in

order for the sensors to provide measurements. Visible/infrared two inch diameter flat mirrors are used to redirect the beam to different components of the testbed.

## **H. SCIENCE CAMERA**

A black and white CCD science camera is used to observe the object source after it has passed through the optical components. A filter is used to filter out the red reference laser light source, leaving only the object source. The camera is model number IV-BWCAM3 manufactured by Industrial Vision Source. The camera has a 1/3 inch 410,000 pixel CCD and an electronic shutter that can operate between 60 to 100,000 Hz (Industrial Vision Source, 2004).

## **I. COMPUTER CONTROL**

Three desktop computers are used to operate the testbed. The testbed is broken into three individual control loops operated by three individual computers. The first computer operates the MMDM, which represents the first primary optical surface of the telescope, and a wavefront sensor. The second computer operates the FSMs, PSD, and the science camera and is responsible for simulating and removing jitter. The third computer operates the PDM and second wavefront sensor and is responsible for providing additional corrections to the wavefront.

## **J. DATA ACQUISITION**

The deformable mirrors are controlled using MATLAB. MATLAB interfaces to the deformable mirrors through a MATLAB executable (MEX) .dll developed by Baker Adaptive Optics. A MEX file is a dynamically linked subroutine that is produced from C or Fortran source code (Mathworks, 2007). In this case C source code is converted to a C-MEX file to provide an external interface with the deformable mirrors. The MEX file is used in conjunction with the OKO Technologies MMDM and PDM drivers. The individual mirror actuators can be addressed through MATLAB, and a control signal between 0 and 255 can be applied individually.

The wavefront sensors are also interfaced with MATLAB but use a C-MEX .dll to a memory mapped file. An executable file called BAOGrabActivate.exe, also developed by Baker Adaptive Optics, is used to perform the continuous image capturing directly to the computer RAM via the memory mapped file. This allows MATLAB to interface with the Basler A601f camera through the Basler frame grabber driver using the 1394 firewire port. Using a cooperative, two part data acquisition (.dll and .exe) lends itself to hyper-threaded and multi-core computer processors as each component runs as an independent and different thread, but shares the memory at full speed. The result is that the data acquisition from the Shack-Hartmann wavefront sensors uses only a small percentage of the CPU processor, which is advantageous when introduced into a control loop.

## **K. CALIBRATION AND ALIGNMENT**

The performance of the adaptive optics system is dependent on the reference signal. In this case the reference signal is a planar wavefront produced by the reference laser. To ensure that the wavefront is planar the beam is expanded using the microscope objective and collimated with a lens. The collimation of the beam is checked using a sheer plate.

The collimated beam is required to calibrate the Shack-Hartmann wavefront sensors. The wavefront sensors operate based on the known positions of the lenslets on the Hartmann mask and their alignment with the CCD. To calibrate the wavefront sensor and remove any tip/tilt bias due to the optical components, a collimated beam was passed into the wavefront sensors and a reference image was captured. This reference image is used to measure the phase difference from a planar wave.

The fast steering mirrors are adjusted such that their un-biased rest position allows the reference beam and object beam to pass through the optical system without any tip or tilt. A two inch flat mirror is then adjusted to ensure the reference beam is positioned on the center of the PSD.

## IV. WAVEFRONT ESTIMATION

### A. WAVEFRONT SENSING

Wavefront sensing is required for a closed loop adaptive optic feedback control algorithm. Therefore, the wavefront sensor must have the spatial resolution and speed to be used in a real-time feedback system. This is even more important for a flexible structure where there is a dynamic disturbance. There are two types of wavefront sensing; direct and indirect. In a direct approach, the wavefront is determined explicitly while an indirect approach never represents the explicit wavefront but rather transforms the sensor data to a control signal (Tyson, 1998).

#### 1. Shack-Hartmann Wavefront Sensor

The Shack-Hartmann wavefront sensor output is proportional to the wavefront slope. The wavefront phase is determined from knowledge of the wavefront slopes. The principle of the Shack-Hartmann wavefront sensor is shown through geometry in Figure 12. The Shack-Hartmann wavefront sensor consists of a lenslet array in front of a CMOS sensor. Each hole on the lenslet array acts as an aperture, and since the source light passing through each lenslet is converging, the image produced on the sensor is an array of spots. The array of spots is directly proportional to the local wavefront tilt at each lenslet. The local wavefront slopes,  $\alpha_{ij}$  and  $\beta_{ij}$ , correspond to the x and y direction respectively. The slope can be determined by the Shack-Hartmann measurements corresponding the lateral shifts,  $\Delta x_{ij}$  and  $\Delta y_{ij}$ , of the local focal point on the sensor. Equations (4.1) and (4.2) describe this relationship where  $\lambda$  is the wavelength of the reference light source, and  $f$  is the focal length of the lenses in the lenslet array (Zhu, Sun, Bartsch, Freeman & Fainman, 1999).

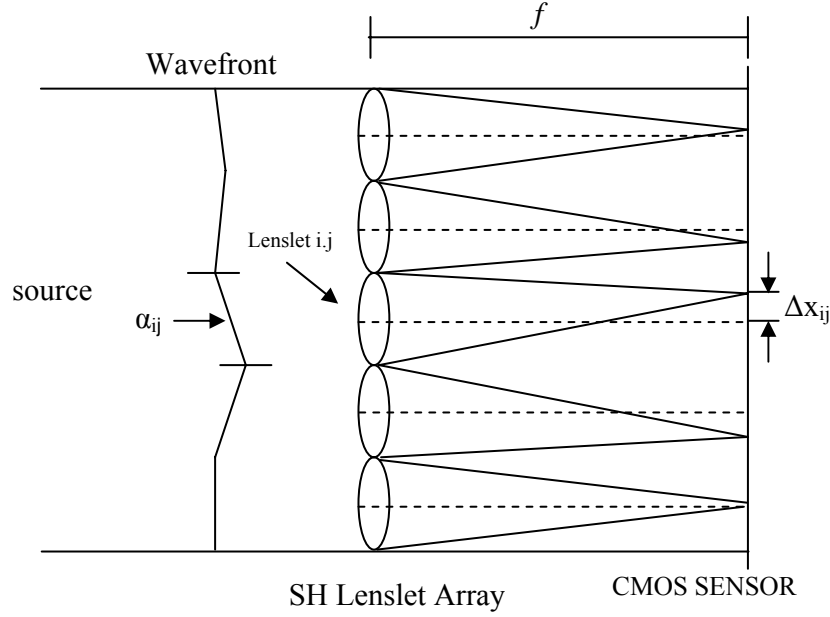


Figure 12 Shack-Hartmann Wavefront Sensor (After, Southwell, 1980)

$$\alpha_{ij} = \frac{2\pi}{\lambda f} \Delta x_{ij} \quad (4.1)$$

$$\beta_{ij} = \frac{2\pi}{\lambda f} \Delta y_{ij} \quad (4.2)$$

The phase can be determined by numerical techniques if the number of slope measurements,  $M$ , is greater than the number of unknown phase points. This creates an over determined problem and a solution can be found through a direct least squares method. The error between the actual phase and the estimated phase determines the physical limitation of the adaptive optics system, and will affect the overall performance of the closed loop feedback control.

## 2. Zernike Polynomials

Optical phase can be represented as a two dimensional surface over the aperture. Deviation from a reference surface is considered the wavefront error. The reference surface used in the experimental work is a planar wavefront. To interpret optical test results it is easy to represent the wavefront as a polynomial series. The polynomial series

is shown in Equation (4.3) where the Zernike coefficients,  $A_{nm}$  and  $B_{nm}$ , completely describe the wavefront up to the order specified by the largest  $m$  and  $n$  (Frazier and Tyson, 2004).

$$\phi(r, \theta) = A_{00} + \frac{1}{\sqrt{2}} \sum_{n=2}^{\infty} A_{n0} \Re_n^0\left(\frac{r}{R}\right) + \sum_{n=1}^{\infty} \sum_{m=1}^n (A_{nm} \cos(m\theta) + B_{nm} \sin(m\theta)) \Re_n^m\left(\frac{r}{R}\right) \quad (4.3)$$

where,

$$\Re_n^0\left(\frac{r}{R}\right) = \sum_{s=0}^{\frac{n-m}{2}} (-1)^s \frac{(n-s)!}{s! \left(\frac{n+m}{2} - s\right)! \left(\frac{n-m}{2} - s\right)!} \left(\frac{r}{R}\right)^{n-2s}$$

The series is in polar coordinates and the radius,  $r$ , is normalized to the unit circle,  $\left(\frac{r}{R}\right)$ , where  $R$  is the aperture radius. Zernike polynomials are orthogonal over the interior of a unit circle, and therefore appropriate for optical surfaces with circular apertures. Zernike polynomials can be transformed to Cartesian coordinates through the relationship,  $r = \sqrt{x^2 + y^2}$ , and  $\theta = \arctan\left(\frac{y}{x}\right)$ . Table 3 shows the first 24 Zernike polynomial terms using Cartesian coordinates.

#	n	m	Polynomial	Term
0	0	0	1	Piston
1	1	1	$x$	X-Tilt
2	1	1	$y$	Y-Tilt
3	1	0	$-1 + 2(x^2 + y^2)$	Focus
4	2	2	$x^2 - y^2$	Astigmatism plus defocus
5	2	2	$2xy$	Astigmatism plus defocus
6	2	1	$-2x + 3x(x^2 + y^2)$	Coma
7	2	1	$-2y + 3y(x^2 + y^2)$	Tilt
8	2	0	$1 - 6(x^2 + y^2) + 6(x^2 + y^2)^2$	Third-Order Spherical and Focus
9	3	3	$x^3 - 3xy^2$	Fifth-Order Aberration
10	3	3	$3x^2y - y^3$	Fifth-Order Aberration
11	3	2	$-3x^2 + 3y^2 + 4x^2(x^2 + y^2) - 4y^2(x^2 + y^2)$	Fifth-Order Aberration
12	3	2	$-6xy + 8xy(x^2 + y^2)$	Fifth-Order Aberration
13	3	1	$3x - 12x(x^2 + y^2) + 10x(x^2 + y^2)^2$	Fifth-Order Aberration
14	3	1	$3y - 12y(x^2 + y^2) + 10y(x^2 + y^2)^2$	Fifth-Order Aberration
15	3	0	$-1 + 12(x^2 + y^2) - 30(x^2 + y^2)^2 + 20(x^2 + y^2)^3$	Fifth-Order Aberration
16	4	4	$x^4 - 6x^2y^2 + y^4$	Seventh-Order Aberration
17	4	4	$4x^3y - 4xy^3$	Seventh-Order Aberration
18	4	3	$-4x^3 + 12xy^2 + 5x^3(x^2 + y^2) - 15xy^2(x^2 + y^2)$	Seventh-Order Aberration
19	4	3	$-12x^2y + 4y^3 + 15x^2y(x^2 + y^2) - 5y^3(x^2 + y^2)$	Seventh-Order Aberration
20	4	2	$6x^2 - 6y^2 - 20x^2(x^2 + y^2) + 20y^2(x^2 + y^2) + 15x^2(x^2 + y^2)^2 - 15y^2(x^2 + y^2)^2$	Seventh-Order Aberration
21	4	2	$12xy - 40xy(x^2 + y^2) + 30xy(x^2 + y^2)^2$	Seventh-Order Aberration
22	4	1	$-4x + 30x(x^2 + y^2) - 60x(x^2 + y^2)^2 + 35x(x^2 + y^2)^3$	Seventh-Order Aberration
23	4	1	$-4y + 30y(x^2 + y^2) - 60y(x^2 + y^2)^2 + 35y(x^2 + y^2)^3$	Seventh-Order Aberration
24	4	0	$1 - 20(x^2 + y^2) + 90(x^2 + y^2)^2 - 140(x^2 + y^2)^3 + 70(x^2 + y^2)^4$	Seventh-Order Aberration

Table 3 24 Terms of Zernike Polynomials (From, Wyant, 2003)



## B. WAVEFRONT ESTIMATION FROM WAVEFRONT SLOPE

Methods for determining the phase of the wavefront are described as either zonal or modal. The methods are simply two different models used to describe the local slope measurements of a Shack-Hartmann wavefront sensor. A zonal method estimates a phase value in a local zone while the modal method is based on a coefficient of an aperture function. In both cases least-squares estimation is used for the phase reconstruction and wavefront estimation.

### 1. Zonal Estimation

If the wavefront is described in optical path distance over a small area or zone then the wavefront is considered zonal (Tyson, 1998). The zonal estimation method is adapted for a specific sensor configuration, as the slope calculations depend on the grid pattern which is then used to determine the phase. For a Shack-Hartmann wavefront sensor a grid configuration is shown in Figure 13. The dots represent the lenslet location while the lines represent the x and y slopes. Each lenslet of the Shack-Hartmann mask measures both the x and y slope at the same point. The wavefront can be determined from slope measurements through a least squares fit of the slope to a model of the phase given at the grid points or zone. The phase can be modeled by assuming the phase difference between two grid points in the x and y direction is represented by the following two polynomials.

$$\phi = c_0 + c_1x + c_2x^2 \quad (4.4)$$

$$\phi = c_0 + c_1y + c_2y^2 \quad (4.5)$$

The slope is calculated by taking the derivative of the previous equations.

$$S^x = c_1 + 2c_2x \quad (4.6)$$

$$S^y = c_1 + 2c_2y \quad (4.7)$$

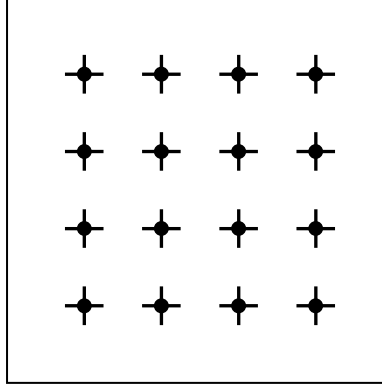


Figure 13 Southwell Geometry, Square Hartmann Mask (After, Southwell, 1978)

The Shack-Hartmann sensor gives two slope measurements per grid point, enabling the determination of both  $c_1$  and  $c_2$  in (4.6) and (4.7). The relationship between slope and phase is given below where the parameter  $h=D/N$  where  $D$  is the diameter of the aperture and  $N$  represents the number of lenslets. Each phase point represents an equal sub-region of the area,  $h^2$ , in the aperture. The following equations are used for a square Hartmann mask (Southwell, 1980).

$$\frac{(S_{i+1,j}^x + S_{ij}^x)}{2} = \frac{(\phi_{i+1,j} - \phi_{i,j})}{h}, \text{ where } \begin{matrix} i=1, N-1 \\ j=1, N \end{matrix} \quad (4.8)$$

$$\frac{(S_{i+1,j}^y + S_{ij}^y)}{2} = \frac{(\phi_{i,j+1} - \phi_{i,j})}{h}, \text{ where } \begin{matrix} i=1, N \\ j=1, N-1 \end{matrix} \quad (4.9)$$

The Hartmann mask used in the experimental setup is a 127 lenslet hexagonal mask with a total aperture of 3.5 mm, as shown in Figure 14. Slope and phase can be related in similar manner using the hexagonal mask as the square mask. However, specific attention must be given to the indexing of the lenslets. Slope averages and phase differences in the x direction are calculated by row using adjacent lenslets. Slope averages and phase differences in the y direction are calculated using lenslets that

are aligned vertically. The lenslets are indexed left to right beginning with the top left lenslet. Equations (4.10) and (4.11) relate slope and phase for the 127 lenslet hexagonal Hartmann mask.

$$\frac{(S_{i+1+k}^x + S_{i+k}^x)}{2} = \frac{(\phi_{i+1+k} - \phi_{i+k})}{h}, \text{ where } \left( \begin{array}{l} i = 1 \text{ to } 114 \\ i \leq 6, k=0 \\ 7 \leq i \leq 13, k=1 \\ 14 \leq i \leq 21, k=2 \\ 22 \leq i \leq 30, k=3 \\ 31 \leq i \leq 40, k=4 \\ 41 \leq i \leq 51, k=5 \\ 52 \leq i \leq 63, k=6 \\ 64 \leq i \leq 74, k=7 \\ 75 \leq i \leq 84, k=8 \\ 85 \leq i \leq 93, k=9 \\ 94 \leq i \leq 101, k=10 \\ 102 \leq i \leq 108, k=11 \\ 109 \leq i \leq 114, k=12 \end{array} \right) \quad (4.10)$$

$$\frac{(S_{i+k+p}^y + S_{i+p}^y)}{2} = \frac{(\phi_{i+k+p} - \phi_{i+p})}{h}, \text{ where } \left( \begin{array}{l} i = 1 \text{ to } 102 \\ i \leq 7, k=16, p=0 \\ 8 \leq i \leq 15, k=18, p=0 \\ 16 \leq i \leq 24, k=20, p=0 \\ 25 \leq i \leq 34, k=22, p=0 \\ 35 \leq i \leq 45, k=24, p=0 \\ 46 \leq i \leq 57, k=25, p=0 \\ 58 \leq i \leq 68, k=24, p=1 \\ 69 \leq i \leq 78, k=22, p=3 \\ 79 \leq i \leq 87, k=20, p=5 \\ 88 \leq i \leq 95, k=18, p=7 \\ 96 \leq i \leq 102, k=16, p=9 \end{array} \right) \quad (4.11)$$

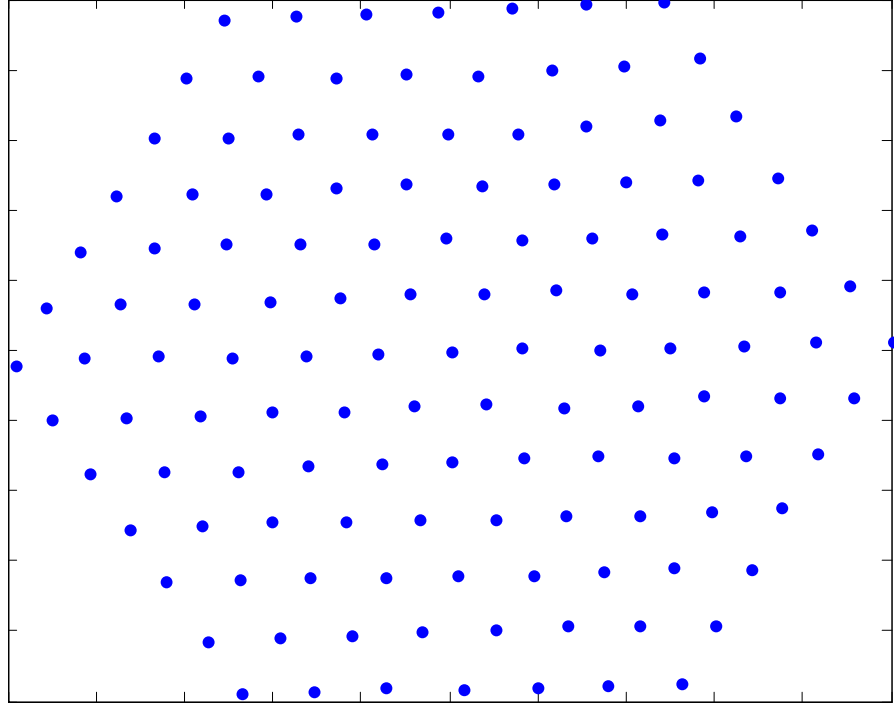


Figure 14 127 Lenslet Hexagonal Hartmann Mask Used in the Adaptive Optics Testbed

A least squares problem can be formulated using the above equations to compute phase from slope. Equation (4.12) represents the least squares problem where  $\underline{S}$  is a vector of slopes,  $\underline{\phi}$  is a vector containing the unknown phase values,  $D$  is a matrix that performs the adjacent slope averaging, and  $A$  is a matrix that computes the phase difference between two grid points. The unknown phase values can be determined by taking the pseudo inverse of  $A$ , represented by  $A^\dagger$ , and pre-multiplying the right and left hand side of Equation (4.12) resulting in Equation (4.13).

$$DS = A\underline{\phi} \quad (4.12)$$

$$\underline{\phi} = A^\dagger D\underline{S} \quad (4.13)$$

## 2. Modal Estimation

A wavefront that is described by coefficients of the modes of a polynomial expansion over the pupil is considered modal (Tyson, 1998). Using the slope measurements from the Shack-Hartmann wavefront sensor a set of coefficients,  $a_k$ , can be obtained that fit the following phase expansion of orthogonal functions. In this case  $z_k(x, y)$  is a set of Zernike polynomials. Zernike polynomials are used as they are a set of orthogonal polynomials over the unit circle. Equation (4.14) can be written as a matrix where the individual phase points that describe the wavefront are contained in the vector  $\underline{\phi}(x, y)$ , the Zernike coefficients are contained in vector  $\underline{a}$ , and matrix  $Z$  contains a matrix of the Zernike terms evaluated at the phase points  $x$  and  $y$  shown in Equation (4.15).

$$\phi(x, y) = \sum_{k=0}^M a_k z_k(x, y) \quad (4.14)$$

$$\underline{\phi}(x, y) = \underline{a}Z \quad (4.15)$$

The M phase expansion coefficients,  $\underline{a}$ , is solved using a least squares estimation, by taking the pseudo-inverse of  $Z$  at the measured phase points from the Shack-Hartmann wavefront sensor and premultiplying both sides of Equation (4.15) resulting in Equation (4.16). This reduces the numerical complexity of the wavefront estimation, from the number of Shack-Hartmann lenslets to the number of expansion terms used.

$$\underline{a} = Z^\dagger \underline{\phi} \quad (4.16)$$

A slope model can be obtained by differentiating Equation (4.14). The resulting relationship for the slope in the  $x$  and  $y$  direction are shown in Equations (4.17) and (4.18), respectively. This allows the slopes, which are measured by the Shack-Hartmann wavefront sensor to be directly related to the partial derivatives of the Zernike polynomials. Equation (4.17) and can be written in matrix form, as shown in Equation (4.19), where  $\underline{S}$  is a vector of  $x$  and  $y$  slopes with the dimensions  $2N \times 1$  and  $dZ$  is a Matrix of the partial derivatives of the Zernike terms evaluated at each lenslet, having  $2N$  rows and  $M$  columns. The Zernike coefficients can be found by solving the least squares

problem with the solution given in Equation (4.20). The benefit of this model phase estimation is that it does not require a zonal phase estimation as Equation (4.16). However, by differentiating Equation (4.14), the piston component of the phase, coefficient  $a_0$ , can not be determined. This is not of concern, as all the other terms in the expansion have a zero mean, and so will the phase without the piston term (Southwell, 1980).

$$S^x = \sum_{k=1}^M a_k \frac{\partial z_k(x, y)}{\partial x} \quad (4.17)$$

$$S^y = \sum_{k=1}^M a_k \frac{\partial z_k(x, y)}{\partial y} \quad (4.18)$$

$$\underline{S} = [dZ] \underline{a} \quad (4.19)$$

$$\underline{a} = [dZ]^\dagger \underline{S} \quad (4.20)$$

## V. CONTROL METHODS

### A. INFLUENCE MATRIX

The MMDM response is proportional to the square of the voltage, as shown in Equation (5.1), where  $d$  is the distance deflected and  $V$  is the applied control signal. The PDM response is linearly proportional to the control signal, Equation (5.2). To verify this relationship a voltage is applied to each electrode ranging from 0 to 255 while maintaining a 0 control signal on all other electrodes. For each control signal applied the slope of the wavefront is measured and plotted as a function of the control signal for a specific actuator, as shown in Figure 15 and Figure 16. This verifies the linear relationships described in Equations (5.1) and (5.2).

$$d_{MMDM} \propto V_{MMDM}^2 \quad (5.1)$$

$$d_{PDM} \propto V_{PDM} \quad (5.2)$$

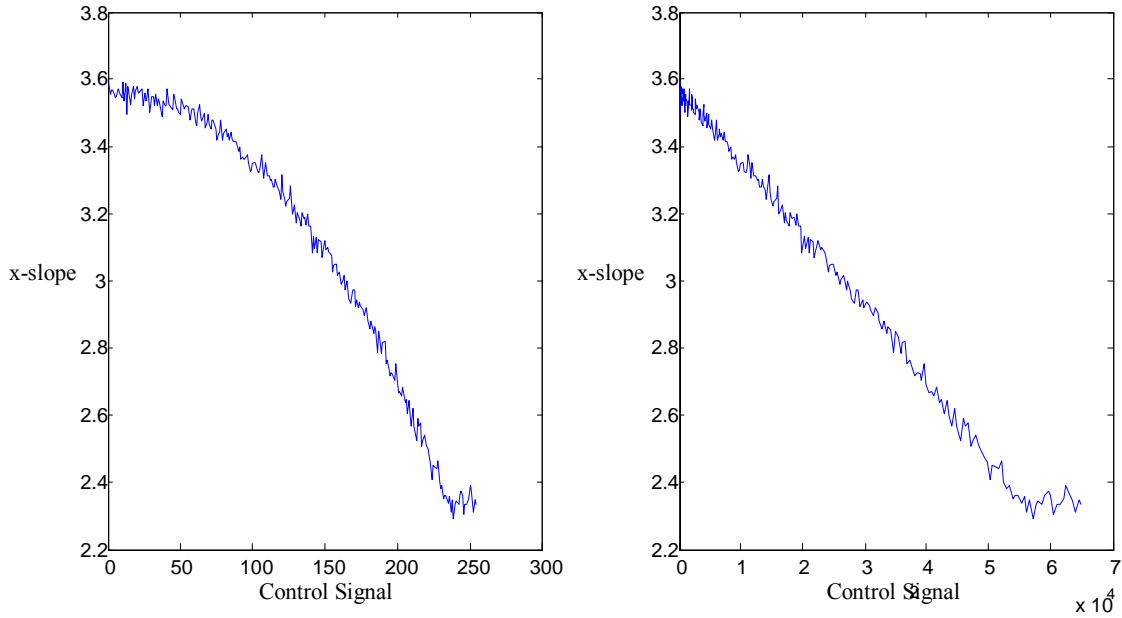


Figure 15 Shack-Hartmann Lenslet 64 X-slope Response vs. MMDM Actuator 1 Control Signal (Left), Shack-Hartmann Lenslet 64 X-slope Response vs. MMDM Actuator 1 Control Signal Squared (Right)

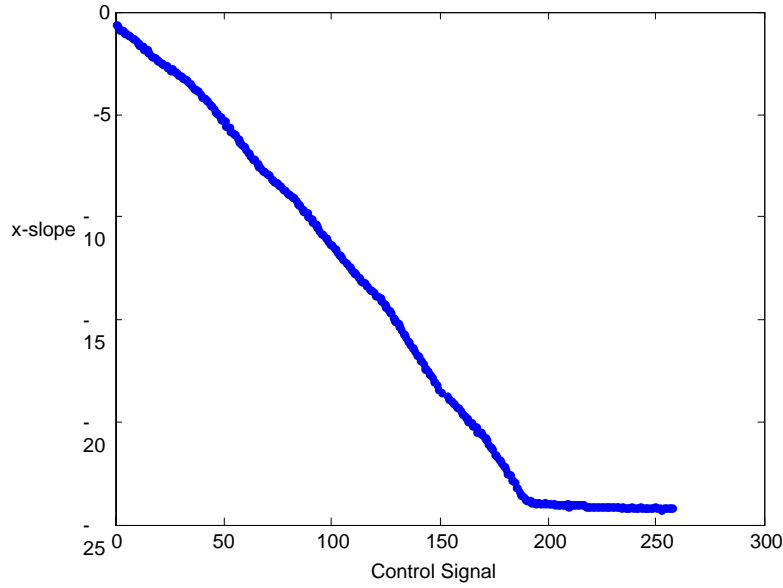


Figure 16 Shack-Hartmann Lenslet 80 X-slope Response vs. PDM Actuator 5 Control Signal

In Figure 15 and Figure 16, the mirror response saturates at higher control signals. The usable control signal range of the mirror is approximately 240 for the MMDM and 190 for the PDM as the surface does not displace with the same linear relationship as it does for lower control signals. These limits must be considered when developing the control law and relating the mirror deformation to a control signal.

To control a deformable mirror, the wavefront sensor data must be related to a control signal in order to provide feedback control in the adaptive optic system. This relationship is established by creating an influence matrix. The influence matrix allows one to relate the control signal of an actuator to the change in the shape of the mirror. The influence matrix is created by setting all the actuator control signals to zero or a biased control signal and applying a maximum control signal to each actuator and recording the response of the wavefront. The influence matrix is also known as a poke matrix as the matrix is built by poking each individual actuator. The wavefront response can be represented indirectly as the sensor response or directly as modal coefficients. The wavefront responses are represented as column vectors for each control channel, and the column vectors make up the influence matrix,  $[B]$ .



The size of the influence matrix depends on the number of sensor measurements,  $N$ , and the number of control channels,  $M$ . The influence matrix takes the form of Equation (5.3), where the column vectors,  $\underline{s}$ , represent the local slopes at each lenslet. Using the Hartmann mask the number of slope measurements equals twice the number of lenslets,  $N$ , as slope is measured in both the  $x$  and  $y$  direction. Each slope vector is defined by Equation (5.4) where the slopes in the  $x$  direction are preceded by the slopes in the  $y$  direction. The resulting influence matrix size for the Shack-Hartmann sensors used in the experimental setup are  $254 \times 37$  and  $254 \times 19$  for the MMDM and PDM respectively.

$$B = [\underline{s}_1 \quad \underline{s}_2 \quad \cdots \quad \underline{s}_M] \quad (5.3)$$

$$\underline{s} = [s_1^x \quad \cdots \quad s_N^x \quad s_1^y \quad \cdots \quad s_N^y]^T \quad (5.4)$$

Once the influence matrix is developed a relationship between control signals and the sensor response can be determined by Equation (5.5), where  $\underline{c}$  is a control signal column vector,  $B$  is the influence matrix and  $\underline{s}$  is a column vector of the sensor data representing local slope measurements at the Shack-Hartmann lenslet. A desired wavefront can be represented as the vector  $\underline{s}$  and the required control signal vector can be computed by taking the pseudo-inverse of the influence matrix using the Singular Value Decomposition (SVD) and pre-multiplying both sides of Equation (5.5) resulting in Equation (5.6). This method computes a least squares solution when determining the control voltage for a desired wavefront.

$$\underline{s} = B_s \underline{c} \quad (5.5)$$

$$\underline{c} = B_s^\dagger \underline{s} \quad (5.6)$$

The influence matrix can be represented using a zonal or modal representation. Instead of representing the Shack-Hartmann data as slopes in the influence matrix the data can be represented as zonal phase points using the phase estimation method described in Equation (4.13). The resulting influence matrix is described by Equation (5.7). The influence matrix can also be represented using a modal phase estimation as described in Equation (4.16) and (4.20) (modes from zonal phase and modes from slope)

resulting in the influence matrix described by Equation (5.8), where  $Z_k$  is a matrix of the Zernike terms evaluated at each phase point. In the experimental setup the matrix  $Z_k$  has the dimensions  $N \times M$ , where  $M$  is the number of Zernike terms used, and the matrix  $dZ$  has the dimensions  $2N \times M$ . In both the zonal and modal representation the relationship between the control voltage and measured wavefront are shown in Equations (5.5) and (5.6). Using a zonal or modal phase representation of the wavefront results in the voltage to wavefront relationship shown in Equations (5.9) and (5.10).

$$B_\phi = A^\dagger DB_s \quad (5.7)$$

$$B_a = Z_k^\dagger A^\dagger DB_s \text{ or } B_a = dZ^\dagger B_s \quad (5.8)$$

$$\underline{c} = B_\phi^\dagger \underline{\phi} \quad (5.9)$$

$$\underline{c} = B_a^\dagger \underline{a} \quad (5.10)$$

Particular attention should be given to the condition number of the influence matrix,  $\kappa = \frac{\sigma_{\max}}{\sigma_{\min}}$ , where  $\sigma$  represents a singular value. A poorly conditioned matrix leads to numerical instabilities when inverting the influence matrix to determine the control signals as in Equation (5.6). Table 4 shows the condition numbers of three influence matrices. The first influence matrix is constructed from sensor slopes, the second from zonal phase points, and the third from modal Zernike coefficients. The condition numbers were obtained experimentally using the MMDM, indicating that the influence matrix with modal coefficients is the most numerically stable.

Influence Matrix	Dimensions	$\kappa$
$B_s$	254 x 37	$6.7 \times 10^4$
$B_\phi$	127 x 37	$6.7 \times 10^3$
$B_a$	21 x 37	221.8

Table 4 Experimental Condition Number of Influence Matrix for MMDM

## B. ITERATIVE FEEDBACK CONTROL

The first controller discussed is used throughout adaptive optics and involves using an iterative closed loop feedback controller. The controller is similar to a closed loop proportional discrete time integral controller where a new control signal is updated based off the error multiplied by a proportional gain. The error is computed using the sensor data which is used to estimate the wavefront and compute the estimated residual wavefront aberration. The residual wavefront aberration is related to a control signal using the influence matrix. The control signal representing the error is then multiplied by a gain. The block diagram is shown below and the plant is represented by the influence matrix  $B$ , which models both the deformable mirror and the wavefront sensor. This control law is implemented using different direct wavefront estimation techniques previously discussed as well as using indirect wavefront representation.

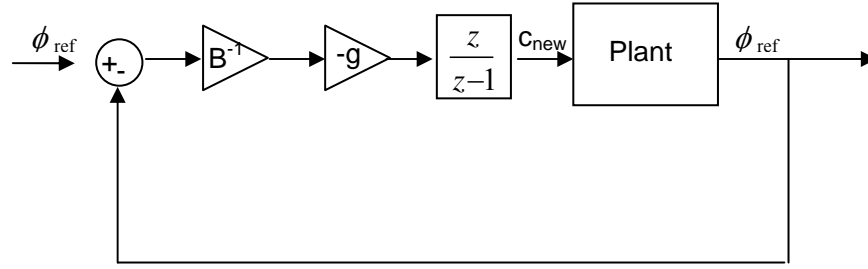


Figure 17 Iterative Feedback Control

### 1. Indirect Iterative Feedback Control

An indirect control method in adaptive optics avoids explicitly determining the wavefront. This can reduce the number of numerical steps in the control algorithm, but may create a poorly conditioned numerical problem. The slope data measured by the Shack-Hartmann wavefront sensor can be directly implemented into a feedback control algorithm. A simple feedback control algorithm is presented in Equation (5.11). This algorithm is an iterative feedback control loop that constantly updates the control signal vector,  $\underline{c}$ , based on a slope measurement vector,  $\underline{s}_s$ , and the influence matrix,  $B_s$ . The

variable  $g$  is a gain between zero and one. The influence matrix is constructed using a biased rest voltage for the actuators not being poked. The influence matrix is inverted using a pseudo-inverse SVD approach.

$$\underline{c}_{n+1} = \underline{c}_n - gB_s^\dagger(\underline{s}_n) \quad (5.11)$$

## 2. Indirect Iterative Feedback Control with Singularity Robust Inverse

The algorithm in Equation (5.11) can experience numerical instabilities when inverting the influence matrix  $B_s$ . If the rank of  $B_s$  (matrix size  $2N \times M$ ) is less than the minimum of  $(2N, M)$ , then  $\det(B_s B_s^T) = 0$ , and a pseudo inverse does not exist. If  $B_s$  is full rank and has a small singular value, the inverse may be poorly conditioned. The pseudo inverse solution also known as the Moore-Penrose inverse solution is used in Equation (5.6), where  $B_s^\dagger = B^T (BB^T)^{-1}$ , which minimizes the 2-norm solution of the following constrained minimization problem, shown in Equation (5.12).

$$\begin{aligned} \min_{\underline{c}} \|\underline{c}\|^2 \quad \text{subject to } B_s \underline{c} = \underline{s} \\ \text{where, } \|\underline{c}\|^2 = \underline{c}^T \underline{c} \end{aligned} \quad (5.12)$$

The pseudo-inverse is a special case of the weighted minimum 2-norm solution where a weighting matrix is included in the minimization problem, resulting in the following problem formulation.

$$\begin{aligned} \min_{\underline{c}} \|\underline{c}\|^2 \quad \text{subject to } B_s \underline{c} = \underline{s} \\ \text{where, } \|\underline{c}\|_Q^2 = \underline{c}^T Q \underline{c} \text{ and } Q = Q^T > 0 \end{aligned} \quad (5.13)$$

$$B_s^\dagger = Q^{-1} B^T (BQ^{-1} B^T)^{-1} \quad (5.14)$$

If a matrix is not full rank or if the matrix is poorly conditioned, an inverse solution can found using a 2-norm and least squares minimization problem, where P and

Q are positive definite weighting matrices (Wie, 2001). A singularity robust inverse is obtained using Equation (5.16). For the experimental setup, the dimensions of P will be  $2N \times 2N$  and the dimensions of Q will be  $M \times M$ .

$$\min_{\underline{c}} \left\{ (B_s \underline{c} - \underline{s})^T P (B_s \underline{c} - \underline{s}) + \underline{c}^T Q \underline{c} \right\} \quad (5.15)$$

$$\underline{c} = B_s^\# \underline{s} \quad (5.16)$$

where,  $B_s^\# = \left[ B_s^T P B_s + Q \right]^{-1} B_s^T P$  and  $\left[ B_s^T P B_s + Q \right]$  is positive definite

Therefore the resulting control law can be written as (5.17). In addition to adjusting the gain, g, the weighting matrices can also be adjusted. The P and Q matrices are assumed to be diagonal matrices. However, the diagonal values can be adjusted to weight the error and control. The error is weighted using the P matrix while the controls are weighted by the Q matrix. By adjusting the P and Q matrices the stability of the system response can be tuned experimentally.

$$\underline{c}_{n+1} = \underline{c}_n - g \left( \left[ B_s^T P B_s + Q \right]^{-1} B_s^T P \right) \underline{s}_n \quad (5.17)$$

### 3. Direct Iterative Zonal Feedback Control

The iterative feedback control law can be implemented using a direct zonal representation of the wavefront in the influence matrix and in the feedback resulting in Equation (5.18). This method reduces the size of the influence matrix to a  $N \times P$  matrix and reduces the column vector,  $\underline{\phi}_n$ , to  $N \times 1$ . One advantage of this method over the indirect method is that the sensor data has a physical meaning at each measured phase point. This method of wavefront estimation is analogous to a finite element approach, where if the number of phase points approached infinity the wavefront would be represented exactly. The challenge with this control algorithm is that the controller is only as good as the zonal phase estimation. Typically the A matrix, which relates measured slopes to phase, is very poorly conditioned resulting in a poor wavefront estimation.

$$\underline{c}_{n+1} = \underline{c}_n - g B_\phi^\dagger (\underline{\phi}_n) = \underline{c}_n - g \left[ A^\dagger D B \right]^\dagger (\underline{\phi}_n) \quad (5.18)$$

#### 4. Direct Iterative Modal Feedback Control

The iterative modal feedback control law represents the influence matrix and sensor data as the modal coefficients of the Zernike polynomial given as the vector  $a_k$ . The modal coefficients are calculated using the zonal phase representation. This method combines the indirect iterative feedback control algorithm with both zonal and modal phase estimation. The addition of the zonal to modal conversion adds additional computations to the algorithm, but also improves wavefront estimation by optimally fitting the zonal phase estimation to a polynomial. One benefit to this approach is the ability to interpret the wavefront easily as Zernike terms. Additionally the influence matrix,  $B_{a_k}$ , is often well conditioned improving numerical stability when inverting the influence matrix.

$$\underline{c}_{n+1} = \underline{c}_n - g B_{a_k} \underline{a}_k = \underline{c}_n - g \left[ Z_k^\dagger A^\dagger D B_s \right]^\dagger \underline{a}_k \quad (5.19)$$

The modal approach can be used with a reduced number of numerical calculations by applying the slope model described in Equations (4.17) to (4.20). This allows the modal coefficients to be computed without zonal phase estimation. The slopes are related to the gradient of the Zernike polynomials and the coefficients are solved using a least squares approach. This method is more numerically stable as there are fewer matrix inversions required in the wavefront estimation portion of the control law.

$$\underline{c}_{n+1} = \underline{c}_n - g B_d \underline{a}_k = \underline{c}_n - g \left[ dZ^\dagger B_s \right]^\dagger \underline{a}_k \quad (5.20)$$

#### C. ITERATIVE GRADIENT FEEDBACK CONTROL

The second controller iteratively adjusts the control signals to reduce the variance of the wavefront or the variance of the slope measurements. This is done by taking the derivative of the variance with respect to the control signal to compute an updated control signal. This controller is similar to the previous controller except the gain is computed by calculating the derivative of the variance.

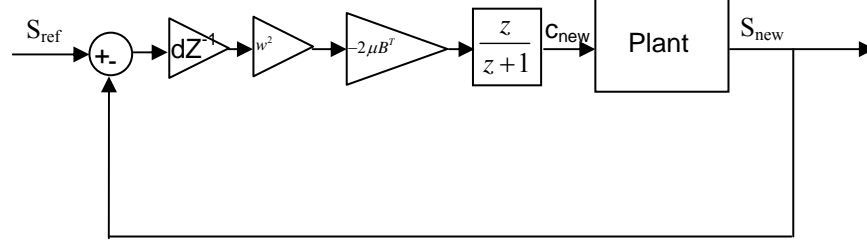


Figure 18 Iterative Gradient Feedback Control

### 1. Direct Gradient Approach

A direct control method developed by Zhu, Sun, Bartsch, and Freeman begins by representing the surface,  $S_0(x, y)$ , of the initial mirror shape using Zernike polynomials, shown in Equation (5.21). The initial surface is computed using the Shack-Hartmann wavefront sensor and determining the Zernike coefficients using the wavefront estimation approaches discussed in Chapter IV. The resulting wavefront is described by a vector of Zernike coefficients. The coefficient vector  $\underline{a}$  is made up of three other coefficient vectors as shown in Equation (5.22). The vector  $\underline{a}_0$  is the initial wavefront coefficients,  $\underline{a}_{in}$  is the input disturbance coefficients, and  $\underline{a}_c$  is the control coefficients computed using Equation (4.16) or (4.20), resulting in the coefficient vector in Equation (5.24).

$$S_0(x, y) = \sum_{k=1}^M a_{0k} z_k(x, y) \quad (5.21)$$

$$\underline{a} = \underline{a}_c + \underline{a}_0 + \underline{a}_{in} = B_a \underline{c} + \underline{a}_0 + \underline{a}_{in} \quad (5.22)$$

$$\underline{a}_{aber} = \underline{a}_0 + \underline{a}_{in} \quad (5.23)$$

$$\underline{a} = B_a \underline{c} + \underline{a}_{aber} \quad (5.24)$$

The cost function of the control algorithm is defined as the wavefront variance over the entire aperture. The variance of the measured wavefront is related to the control signal so that the variance can be reduced iteratively, by adjusting the control signal. The wavefront variance is described over the unit circle for Cartesian coordinates in Equation (5.25). Assuming a planar reference wave,  $\phi_0(x, y)$ , the Zernike polynomial expansion describes the wavefront variance from the planar wave, as shown in Equation (5.26).

Therefore due to the orthogonality of Zernike polynomials, when the wavefront variance is described by Equation (5.26), the wavefront variance,  $\sigma_\phi^2$ , is the sum of individual variances of the  $k^{\text{th}}$  polynomial term,  $\sigma_k^2$ . The error can then be defined as the variance, as shown in Equation (5.27).

$$\sigma_\phi^2 = \frac{1}{\pi} \int_{-1}^1 \int_{-\sqrt{1-x^2}}^{\sqrt{1-x^2}} [\phi(x, y) - \phi_0(x, y)]^2 dx dy \quad (5.25)$$

$$\phi(x, y) - \phi_0(x, y) = \sum_{k=0}^M a_k z_k(x, y) \quad (5.26)$$

$$E = \sigma_\phi^2 = \sum_{k=1}^M \sigma_k^2 \quad (5.27)$$

The variance equation can be rewritten in terms of the Zernike polynomial, Equation (5.28). The Zernike coefficients are constants and can be moved in front of the integrals. Since the Zernike polynomial is valid over the unit circle, the Zernike terms can be integrated numerically over the unit circle resulting in a vector of coefficients,  $\underline{w}_k$ . The error equation can then be rewritten as Equation (5.30), where vectors  $\underline{a}$  and  $\underline{w}$  are the Zernike coefficients of the Zernike terms evaluated over the unit circle respectively. Equation (5.24) can then be substituted into Equation (5.30) resulting in the error Equation (5.31).

$$\sigma_\phi^2 = \frac{1}{\pi} \int_{-1}^1 \int_{-\sqrt{1-x^2}}^{\sqrt{1-x^2}} [a_k z_k(x, y)]^2 dx dy = a_k^2 \frac{1}{\pi} \int_{-1}^1 \int_{-\sqrt{1-x^2}}^{\sqrt{1-x^2}} [z_k(x, y)]^2 dx dy = a_k^2 w_k^2 \quad (5.28)$$

where,

$$\underline{w}_k^2 = \frac{1}{\pi} \int_{-1}^1 \int_{-\sqrt{1-x^2}}^{\sqrt{1-x^2}} [z_k(x, y)]^2 dx dy \quad (5.29)$$

$$E = \sum_{k=1}^M a_k^2 w_k^2 = \|\underline{a} * \underline{w}\|^2 \quad (5.30)$$

$$E = \|(B\underline{c} + \underline{a}_{aber}) * \underline{w}\|^2 \quad (5.31)$$



Equation (5.31) computes the error in terms of a control signal,  $\underline{c}$ , and the measured Zernike coefficients. The vector of Zernike terms is a constant that weights the Zernike coefficients. The error equation is a cost function, and the error can be minimized by taking the derivative of the cost function with respect to the control variable, as shown in Equation (5.32), and the direction of increasing wavefront error with respect to the control signal can be determined. Adjusting the control signal vector in the opposite direction of the increasing wavefront error can reduce the wavefront error, driving the gradient toward zero. An iterative feedback control law can be applied using this approach by updating the control voltage in Equation (5.33), where  $\mu$  is a scalar gain (Zhu, Sun, Bartsch, Freeman & Fainman, 1999). The gain,  $\mu$ , is determined empirically and as the control signals are updated the error will approach a minimum.

$$\frac{\partial E}{\partial \underline{c}} = 2B^T (\underline{a} * \underline{w}^2), \text{ where } \underline{w}^2 = [w_1^2, w_2^2, \dots, w_M^2]^T \quad (5.32)$$

$$\underline{c}_{n+1} = \underline{c}_n - 2\mu B^T (\underline{a} * \underline{w}^2) \quad (5.33)$$

The above algorithm can be optimized and tuned by adjusting the gain,  $\mu$ , and the vector  $\underline{w}^2$ . Faster convergence toward a minimum wavefront error can be achieved by increasing the gain,  $\mu$ , however as the algorithm iterates a large  $\mu$  value may lead to instabilities. Therefore the gain,  $\mu$ , can be adaptively decreased as the error converges toward zero, improving stability by decreasing the step size and preventing large oscillations around the minimum point. The Zernike term vector,  $\underline{w}^2$ , can be adjusted to change the convergence speed of each Zernike term to improve system performance.

One advantage to this algorithm is that a modal disturbance can be input into the system by adding the  $\underline{a}_{in}$  term. This allows individual Zernike modes to be excited. In experimental work, a disturbance can be easily added to the system and characterized in terms of the Zernike mode.

## 2. Indirect Gradient Approach

An attractive control method is to combine the gradient approach in the previous section with an indirect approach, eliminating the need to compute a matrix inverse. This is accomplished by redefining the cost function used by Zhu, Sun, Bartsch, and Freeman (Zhu, Sun, Bartsch, Freeman & Fainman, 1999). Instead of defining error as the variance of the wavefront or the aperture, error is defined as the sum of the squares of individual sensor slopes, shown in Equation (5.34). This becomes the cost function to minimize.

The slopes consists of both slopes in the x and y direction, resulting in a column vector with  $2N$  rows. The slope vector,  $\underline{s}$ , is defined by Equation (5.35), where  $\underline{s}_0$  represents the initial slopes and  $\underline{s}_c$  the controlled slopes. The controlled slopes can be computed using the influence matrix and control voltages as shown in Equation (5.5). The error can be expressed as a summation of the slopes in Equation (5.36), and can be expressed using matrices in Equation (5.37), where Equation (5.5) has been substituted for  $\underline{s}_c$ . By taking the derivative of the error with respect to the control voltage results in Equation (5.38), the gradient of the slopes is determined. The derivative of the error is used in an iterative control loop to determine the direction of increasing slope with respect to the control signal, as shown in Equation (5.39), where  $\mu$  is a gain and  $\underline{s}_0$  is a column vector of zeros for a planar wave.

$$E = \sum_{k=1}^{2N} s_k^2 \quad (5.34)$$

$$\underline{s} = \underline{s}_0 + \underline{s}_c \quad (5.35)$$

$$E = \sum_{k=1}^{2N} \left( s_{0_k} + s_{c_k} \right)^2 \quad (5.36)$$

$$E = \left[ \underline{s}_0 + B_s \underline{c} \right]^T \left[ \underline{s}_0 + B_s \underline{c} \right] \quad (5.37)$$

$$\frac{\partial E}{\partial \underline{c}} = 2B_s^T (\underline{s}_0 + B_s \underline{c}) = 2B_s^T (\underline{s}_0 + \underline{s}_c) \quad (5.38)$$

$$\underline{c}_{n+1} = \underline{c}_n - 2\mu B^T \underline{s}_c \quad (5.39)$$

The resulting control law, shown in Equation (5.39), does not require any inverse matrix operations or wavefront estimation. However, a reference slope vector is required when computing the slopes. In this case the reference slope vector is a Shack-Hartmann sensor reading when the wavefront is planar, and therefore  $\underline{s}_0$  is a vector of zeros. The algorithm drives the slopes to zero by changing the control signal, and the resulting wavefront should match the reference wavefront.

#### D. COMBINED ITERATIVE AND GRADIENT FEEDBACK

Another control law is developed by combining the direct iterative feedback control with the gradient feedback control, as shown in Equation (5.40). This control law subtracts the wavefront difference multiplied by a gain and corrects the wavefront by compensating for the change in the wavefront error by taking the derivative. This algorithm should allow wavefront error to converge faster, and also, overcome the inherent local minimum problem with the gradient approach.

$$\underline{c}_{n+1} = \underline{c}_n - gB_a^\dagger \underline{a} - 2\mu B_a^T (\underline{a} * \underline{w}^2) \quad (5.40)$$

#### E. FILTERING

Filtering techniques can be applied to control resonant peaks and known frequencies that excite a structure. This is a potential problem for a large aperture space telescope as the control system may excite the structure. Additionally a structure with low damping may lead to increased resonant peaks in the frequency response of the structure causing potential wavefront error as the aperture surface dynamically changes. External narrowband disturbances are also of concern as they can impart a disturbance on a structure. Notch filters can cancel the narrowband disturbances. Notch filters are characterized by a unit gain at all frequencies except at the sinusoidal frequencies in which their gain is zero (Pei S. C. & Tseng C. C., 1997).'

Second order structural filters can be applied to compensate for known resonant frequencies. The second order structural filter takes the form of Equation (5.41), where

the  $\omega$  and  $\zeta$  terms can be manipulated to achieve phase lead, phase lag, notch, minimum bandpass, non-minimum phase all pass, and non-minimum high and low pass filters. A second order notch filter has the property that all the frequencies are equal,  $\omega_z = \omega_c = \omega_p$ , and the max gain is determined by  $K_{\max} = 20 \log_{10} \left( \frac{\zeta_z}{\zeta_p} \right)$ .

$$G(s) = \frac{\frac{s^2}{\omega_z^2} + \frac{2\zeta_z s}{\omega_z} + 1}{\frac{s^2}{\omega_p^2} + \frac{2\zeta_p s}{\omega_p} + 1} \quad (5.41)$$

In order to implement a notch filter on the experimental testbed a discrete time notch filter is required. A second order notch filter in the Z-domain is presented in Equation (5.42) where  $\omega_n$  and  $BW$  are the normalized central angular frequency and bandwidth of the notch filter (Hsu, Chen & Tsai, 2007). This notch filter can be applied to an individual actuator control signal, requiring a notch filter on each control channel of the deformable mirror to remove known narrowband disturbances. The notch filter is implemented on the testbed using Equation (5.45) where  $y(n)$  represents the current output and  $u(n)$  is the current control input.

$$H_z(z) = \frac{1}{2} \left[ 1 + \frac{k_2 + k_1(1 + k_2)z^{-1} + z^{-2}}{1 + k_1(1 + k_2)z^{-1} + k_2z^{-2}} \right] \quad (5.42)$$

where,

$$k_1 = -\cos(\omega_n) \quad (5.43)$$

$$k_2 = \frac{1 - \tan\left(\frac{BW}{2}\right)}{1 + \tan\left(\frac{BW}{2}\right)} \quad (5.44)$$

$$y(n) = -k_1(1 + k_2)y(n-1) - k_2y(n-2) + \frac{1+k_2}{2}u(n) + k_1(1+k_2)u(n-1) + \frac{(k_2+1)}{2}u(n-2) \quad (5.45)$$

The Bode plot of the notch filter is shown in Figure 19 for a frequency of 5 Hz ( $31.4 \text{ rad/sec}$ ) and a bandwidth of  $0.1\pi$  and  $0.5\pi$ . The performance of the notch filter on the testbed is dependent on the a priori knowledge of the disturbance frequency. The disturbance frequency input into the system is dependent on the sampling time of the computer controller which can vary in the experimental setup. Therefore using a narrow bandwidth may miss the uncertain disturbance frequency. Increasing the bandwidth of the notch filter will help remove the disturbance if the frequency is not exactly known, but will also decrease the gain of the desired control signal.

The notch filter may also be implemented in a cascade fashion to remove multiple frequencies. The Bode plot in Figure 20 shows a cascaded notch filter for 0.8 Hz and 5 Hz at a bandwidth of  $0.1\pi$  and  $0.5\pi$ . At a higher bandwidth of  $0.5\pi$ , the two notch filters begin to overlap causing a gain decrease between the two frequencies. This gain drop will translate to a smaller control signal gain, reducing the overall control influence of the mirror face-sheet.

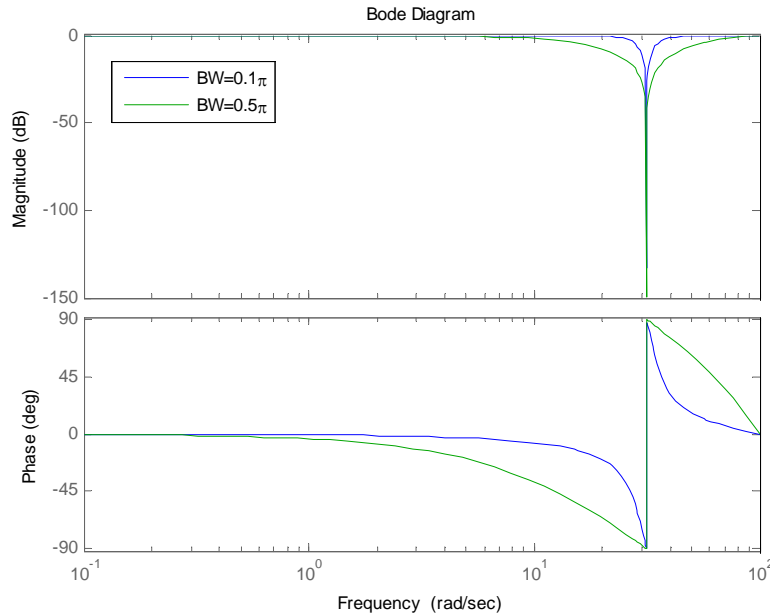


Figure 19 Bode Plot of Discrete Second Order Notch Filter for Different Bandwidths

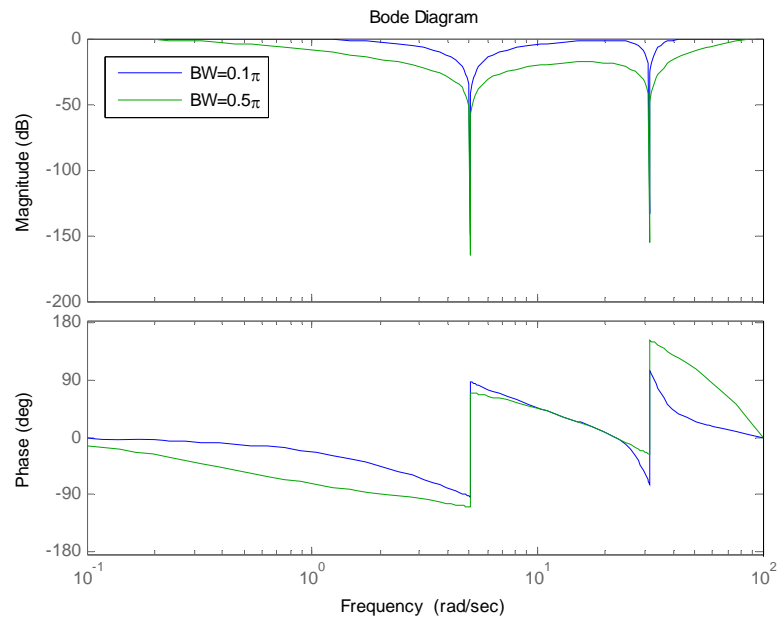


Figure 20 Bode Plot of Cascaded Discrete Second Order Notch Filter for Different Bandwidths

## **VI. ANALYSIS**

### **A. WAVEFRONT CORRECTION**

The adaptive optics testbed is used to verify wavefront correction algorithms. In order to analyze the wavefront two figures of merit are used; peak to valley wavefront aberrations and root mean square (RMS) wavefront error. The RMS wavefront error and peak to valley wavefront aberration is easily computed from a modal phase representation. Therefore to compare results of different control algorithms a standard wavefront estimation method is used when computing error and reconstructing the wavefront.

The standard wavefront estimation algorithm used is the modal phase estimation method described in Equation (4.20) using the derivatives of the Zernike polynomial terms. This method was chosen because the wavefront can be directly estimated from the Shack-Hartmann slope data. The wavefront estimation method only requires one matrix inverse of a well conditioned matrix of orthogonal Zernike terms. A total of 21 Zernike terms are used in the wavefront estimation to compute the RMS wavefront error and peak to valley wavefront aberration.

#### **1. Peak to Valley Wavefront Aberation**

When complicated wavefront aberrations are described in terms of third order aberrations, the piston, tip, and tilt aberration is ignored. The easiest way to describe the wavefront error is in terms of peak to valley wavefront aberrations, measured in waves (Wyant, 2003). This figure of merit describes how far the measured wavefront is from the desired wavefront. This figure of merit is an absolute value of the measured difference from the desired wavefront, similar to an infinity norm. The peak to valley wavefront aberration is calculated using a wavefront estimation technique and summing the absolute value of the maximum and minimum deviation from a planar wavefront.

## 2. RMS Wavefront Error

The use of the peak to valley figure of merit can be misleading as it does not describe the area over which the error occurs (Wyant, 2003). The peak to valley measurement only gives the maximum wavefront error. Another figure of merit that provides a more meaningful measure of wavefront quality is the root mean square (RMS) wavefront error. The RMS wavefront error is the square root of the variance of the wavefront. The variance was described in chapter V and used as a cost function. Therefore by taking the square root of the double integral of the Zernike polynomial over the unit circle the RMS error is computed, using Equation (6.1).

$$\sigma_{\phi} = \sqrt{\frac{1}{\pi} \int_{-1}^1 \int_{-\sqrt{1-x^2}}^{\sqrt{1-x^2}} [a_k z_k(x, y)]^2 dx dy} = \sqrt{a_k^2 \frac{1}{\pi} \int_{-1}^1 \int_{-\sqrt{1-x^2}}^{\sqrt{1-x^2}} [z_k(x, y)]^2 dx dy} = \sqrt{a_k^2 w_k^2} \quad (6.1)$$

### B. SURFACE CORRECTION OF THE MMDM

The control algorithms developed previously were applied to the MMDM to correct the mirror surface from a biased position. This allows the control algorithms to be validated and compared when not subject to a disturbance. A bias control signal of 240 was applied to all the actuators on the MMDM resulting in a peak to valley wavefront aberration of 17.7 waves and RMS wavefront error of 10.96 as shown in Figure 21. In all experimental tests, the control signals were limited between 0 and 240 based on the results from Figure 15. The error of the wavefront is only calculated over 85% of the Hartmann mask aperture using a diameter of 3 mm. This eliminates the outer fringes of the wavefront as the MMDM deformation range is limited at the outer edges since the membrane is fixed at the boundary. The control algorithms were configured to drive the mirror from the biased position to a position resulting in a planar wavefront.



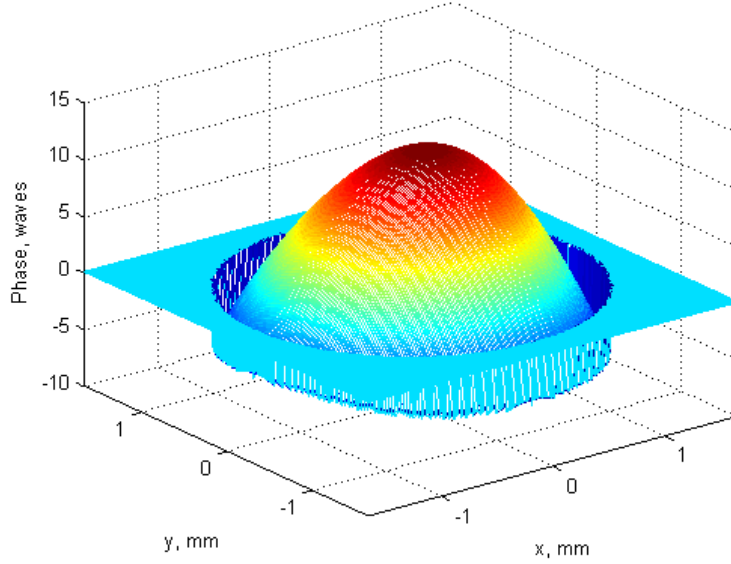


Figure 21 Biased Wavefront of MMDM,  $\sigma = 10.96$ , Peak to Valley = 17.79 waves, Control Signal Equals 240

## 1. Indirect Iterative Control

The indirect iterative control methods include the control algorithms presented in Equations (5.11) and (5.17). The gain is set to 0.9 in both experiments and the loop is run for 150 iterations. Figure 22 and Figure 23 show the wavefront representation of the Fcorrected wavefront after 150 iterations. Both methods improve the biased wavefront, however the singularity robust method outperforms the SVD method by a factor of 10. Both control algorithms are the same except for the matrix inversion algorithm. Figure 24 shows the RMS wavefront error history for the 150 iterations for both algorithms.

The numerical instabilities of inverting the  $254 \times 37$  influence matrix using the SVD inverse are apparent in the error history plot. The jagged peaks seen in the error using the SVD method in Figure 24 indicate an over correction and instability. This can be improved by decreasing the gain. The singularity robust method uses the weighting matrices Q and P to weight the influence of the control and the error. In this experiment the Q matrix is a diagonal matrix of ones with the size  $37 \times 37$ , and the P matrix is a diagonal matrix of 0.01 with the size of  $254 \times 254$ . The stability and performance of the control loop are improved by using the singularity robust inverse.

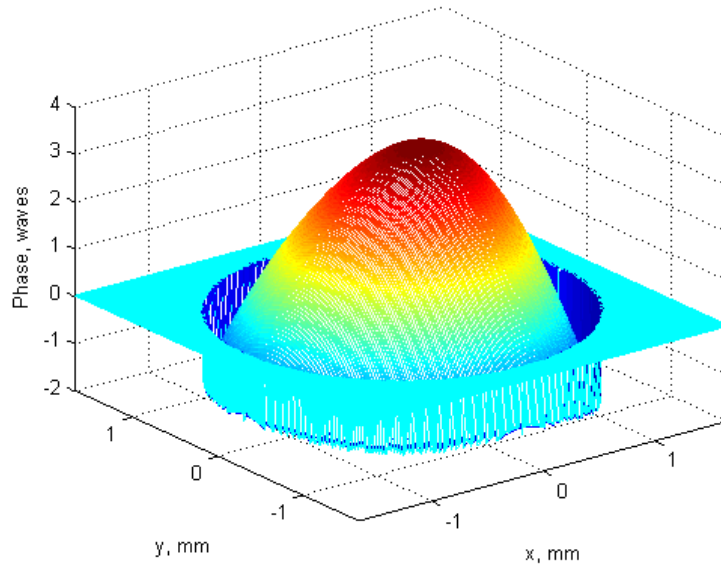


Figure 22 Corrected Wavefront Using Indirect Iterative Feedback Control with Shack-Hartmann Slopes and SVD Inverse, Peak to Valley = 5.42 Waves

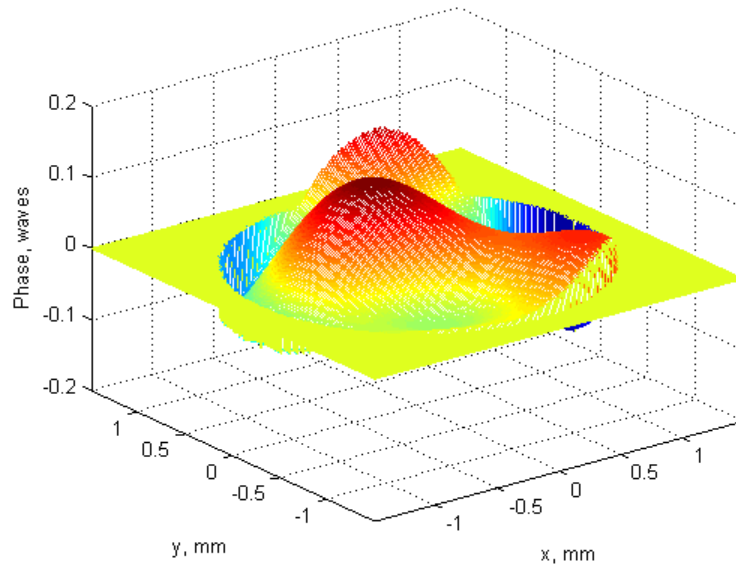


Figure 23 Corrected Wavefront Using Indirect Iterative Feedback Control with Shack-Hartmann Slopes and Singularity Robust Inverse, Peak to Valley = 0.266 Waves

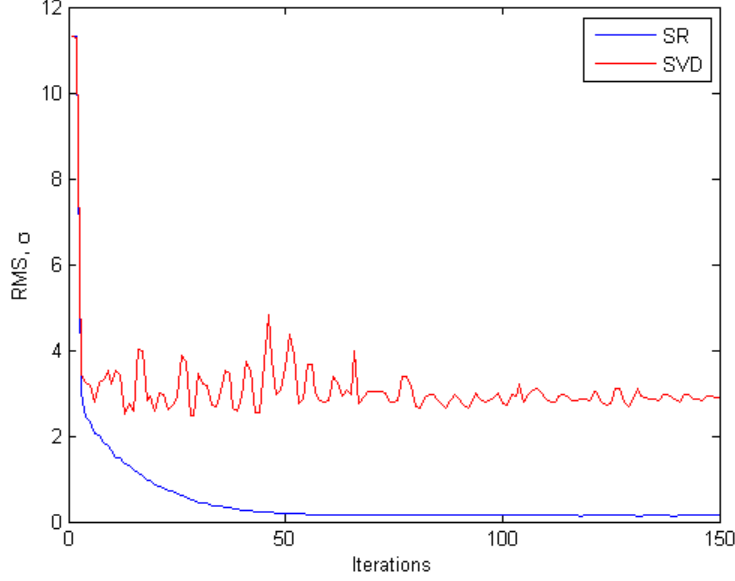


Figure 24 Error History Using Indirect Iterative Feedback Control with Shack-Hartmann Slopes with Singularity Robust Inverse and SVD Inverse

## 2. Direct Iterative Control

Three direct iterative control methods are employed with the difference being the phase representation. The control algorithm in (5.18) uses a zonal phase representation where the wavefront is computed from the Shack-Hartmann slope measurements using a bi-quadratic spline producing the relationship in Equations (4.10) and (4.11) which are modified from the Southwell geometry in Equations (4.8) and (4.9) (Southwell, 1980). The resulting wavefront and error history are shown in Figure 25 and Figure 26. The zonal iterative feedback control algorithm does show improvement from the biased wavefront, but still does a poor job. This is due to the poor condition number,  $\kappa \approx 1 \times 10^{15}$ , of the A matrix that computes the phase difference between two grid points in Equation (4.13). Therefore, the feedback used in the control algorithm,  $\underline{\phi}$ , is not numerically stable and accumulates error. The gain for the control loop is set to 0.2 empirically to provide a stable and fast response.

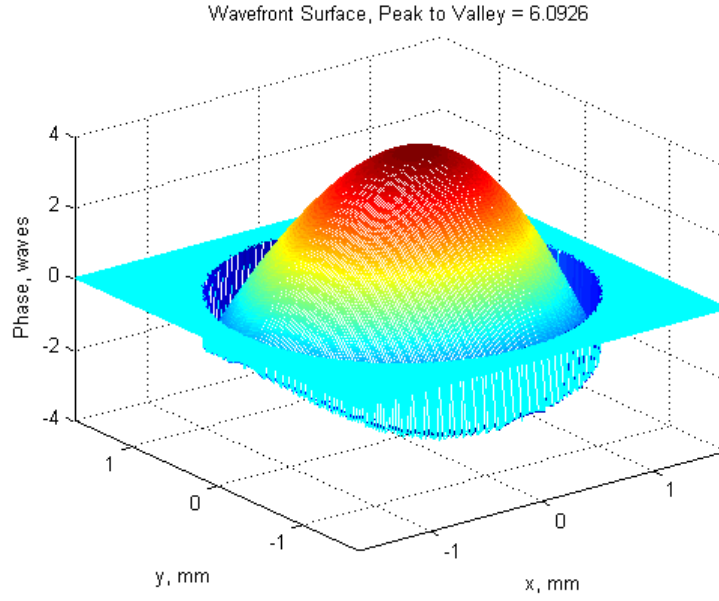


Figure 25 Corrected Wavefront Using Zonal Iterative Feedback Control, Peak to Valley = 6.0926 Waves

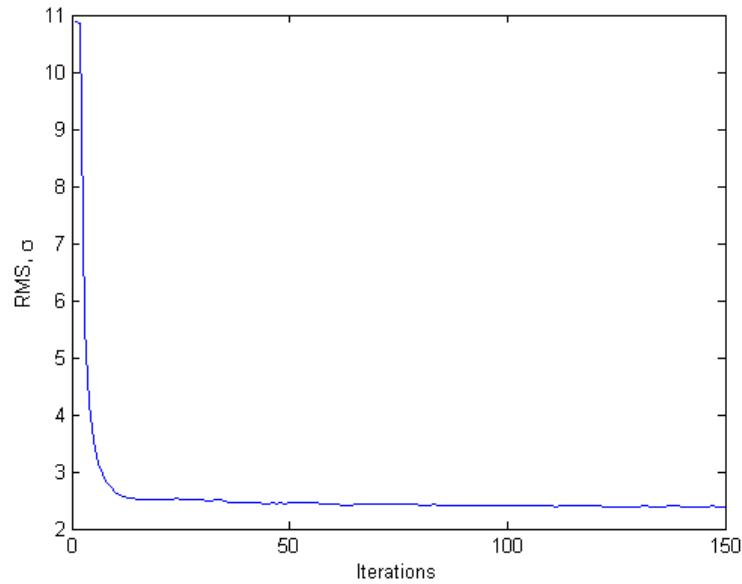


Figure 26 Error History Using Zonal Iterative Feedback Control

The control algorithm in Equation (5.19) uses modal wavefront estimation derived from zonal wavefront estimation. The Zernike coefficients are computed using (4.16) and are used as the feedback to the control algorithm. This method performs significantly better than the previous zonal method. The error present in the zonal

wavefront estimation is reduced as the zonal wavefront is fitted by a least squares technique to 21 Zernike coefficients. The gain for this method was set to 0.4 empirically. This gain produced good results with a stable response and fast convergence.

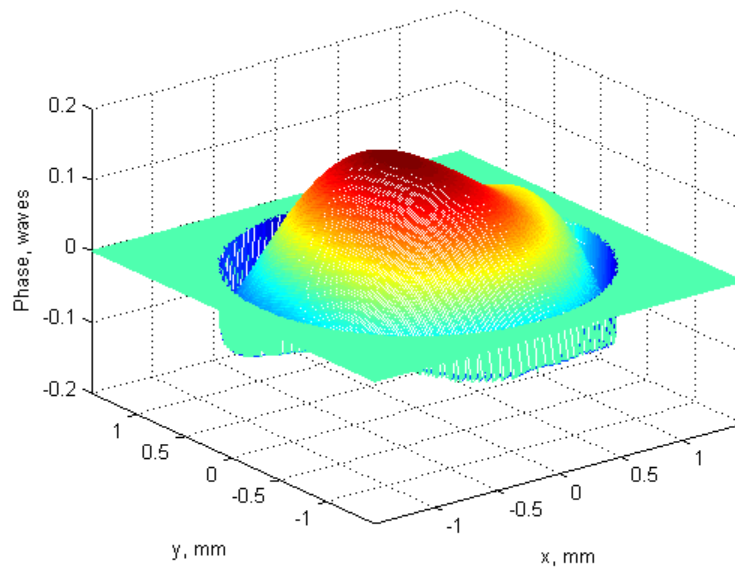


Figure 27 Corrected Wavefront Using Modal (derived from Zonal) Iterative Feedback Control, Peak to Valley = 0.268 Waves.

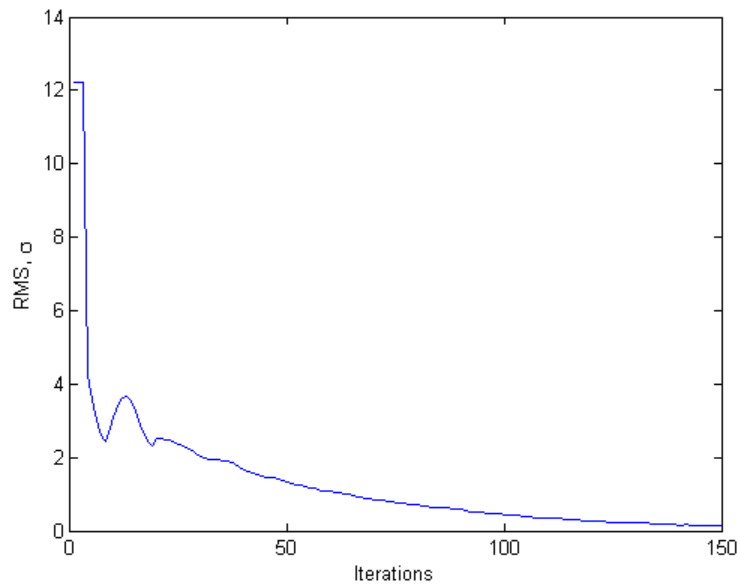


Figure 28 Error History Using Modal (derived from Zonal) Iterative Feedback Control

The third direct iterative control method estimates the wavefront directly from the Shack-Hartmann wavefront sensor slope measurements using the derivatives of the Zernike terms. The control algorithm in Equation (5.20) outperforms the two previous control methods. The gain was set to 0.11 empirically. This provided a stable response that converged relatively fast. The improved performance comes from the simplified wavefront estimation technique. The least squares wavefront estimation requires the matrix inversion of the matrix  $dZ$ , which is well conditioned since it contains the orthogonal Zernike terms, reducing numerical error. The resulting influence matrix is also well conditioned making the control loop numerically stable.

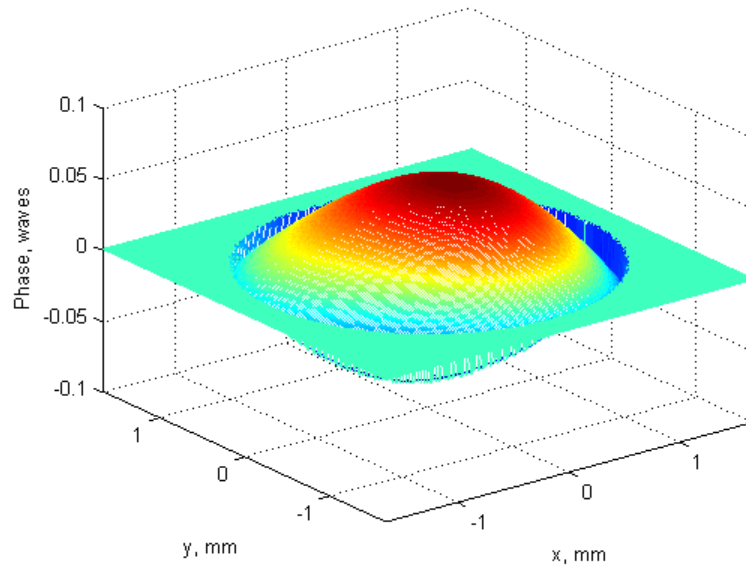


Figure 29 Corrected Wavefront Using Modal (derived from Zernike Derivatives) Iterative Feedback Control, Peak to Valley = 0.0826

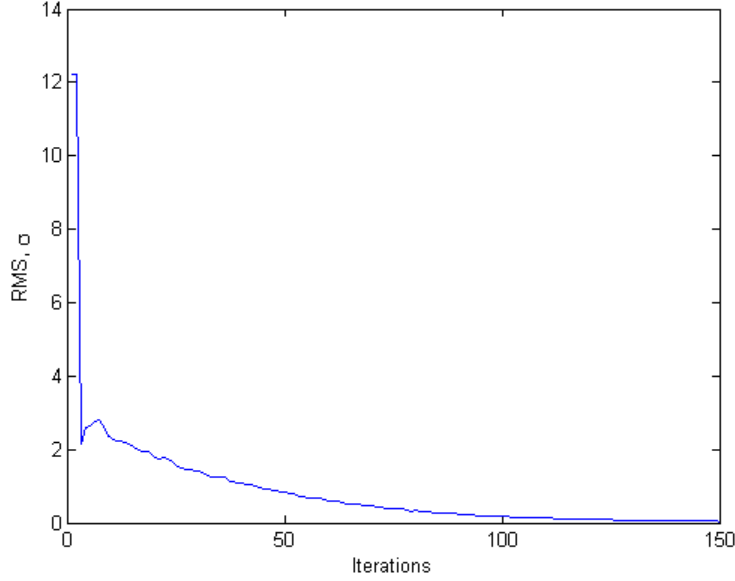


Figure 30 Error History Using Modal (derived Zernike Derivatives) Iterative Feedback Control

### 3. Iterative Gradient Feedback Control

Two iterative gradient feedback control algorithms were implemented using Equations (5.33) and (5.39). The first control algorithm iteratively adjusts the control voltage by minimizing the variance of the wavefront, estimated using the modal estimation method described in (4.20) (Zhu, Sun, Bartsch, Freeman & Fainman, 1999). The gain is empirically set to 0.039. The results in Figure 31 and Figure 32 show a wavefront improvement over the 150 iterations.

The other iterative gradient feedback control algorithm was developed by minimizing the measured slope error. This algorithm does not require wavefront estimation and can be implemented directly from the Shack-Hartmann wavefront sensor feedback. The gain is empirically set to 0.00001. The results in Figure 33 and Figure 34 show wavefront improvement over the 150 iterations outperforming the variance minimization method.

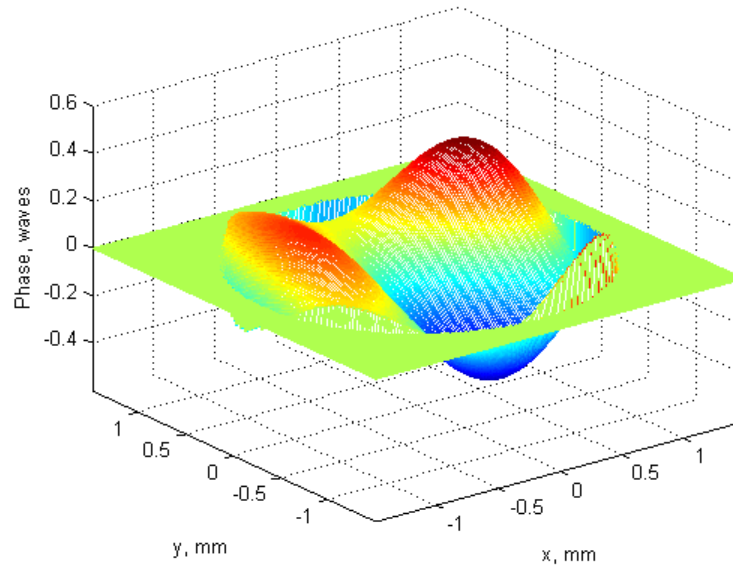


Figure 31 Corrected Wavefront Using Iterative Gradient Feedback Minimizing Wavefront Variance, Peak to Valley = 0.735 Waves

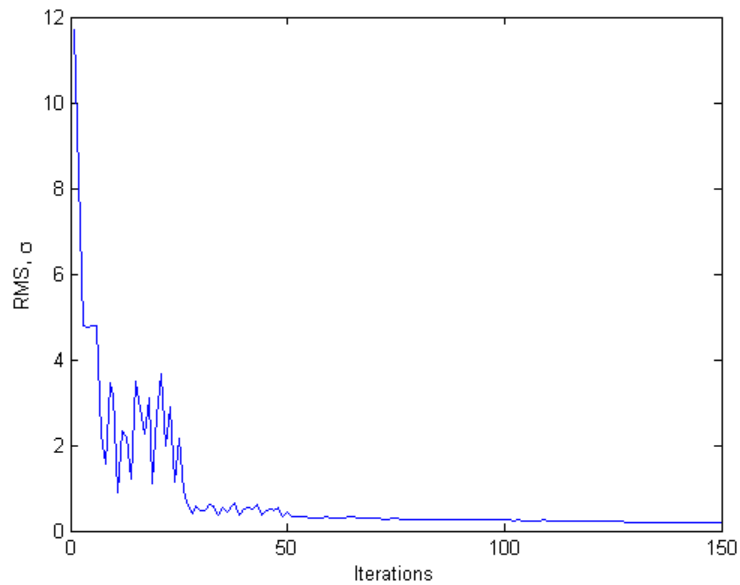


Figure 32 Error History Using Iterative Gradient Feedback Minimizing Wavefront Variance



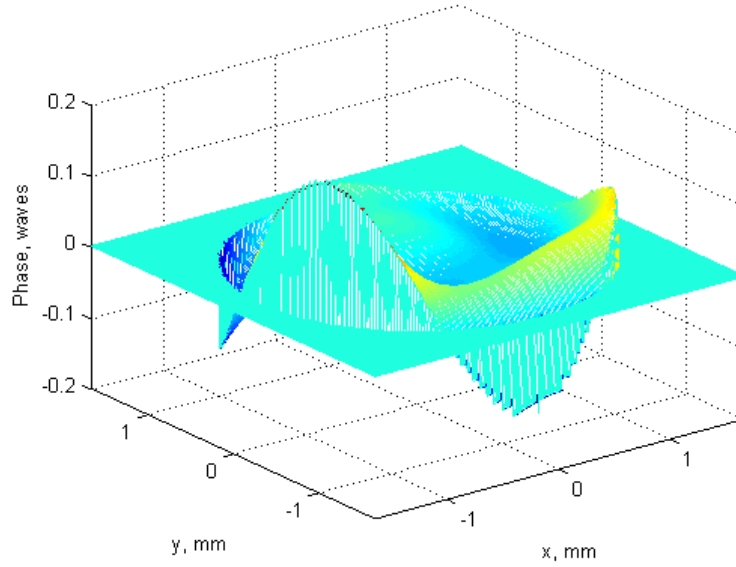


Figure 33 Corrected Wavefront Using Iterative Gradient Feedback Minimizing Slope Error, Peak to Valley = 0.33714

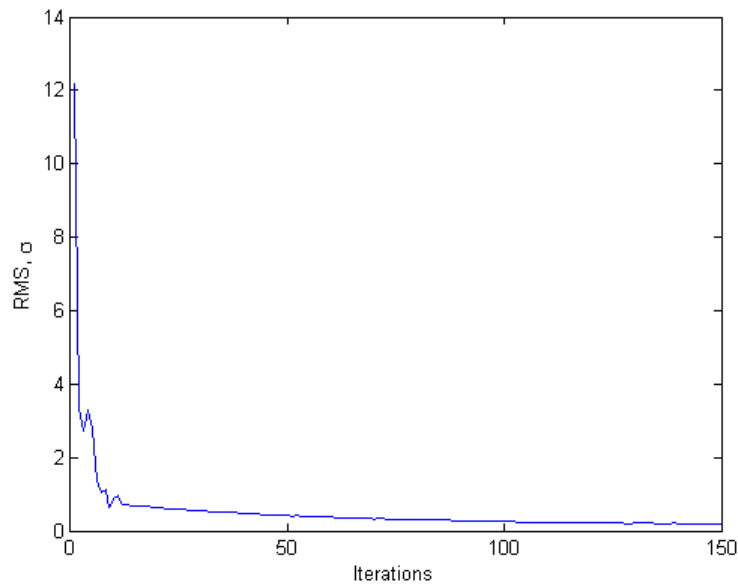


Figure 34 Error History Using Iterative Gradient Feedback Minimizing Slope Error, 150 Iterations

The iterative gradient feedback control algorithms performance can be improved by adjusting the gain and adjusting the Zernike coefficient weighting vector,  $w^2$ , for Equation (5.33). This can improve the convergence speed as well as the wavefront error

in both algorithms. One inherent problem with gradient methods is that a global minimum is not guaranteed. Therefore, the algorithm may drive the wavefront to a local minimum, limiting the performance of the algorithm.

In the two proposed gradient methods the gain must be determined empirically to control the step size of control voltage change for each iteration. If the step size is too large an oscillatory response may develop as the mirror oscillates around a local minimum. Using the previous iterative feedback methods, the gain is between 0 and 1 because the control law is based on an influence matrix that is built using a control signal between 0 and 1, making the controller easier to tune.

#### **4. Combined Iterative and Gradient Feedback Control**

The direct iterative feedback control law using Zernike modes estimated from Zernike derivatives is combined with the direct gradient feedback minimizing the variance control law. The results were compared against the direct iterative feedback control law using Zernike coefficients estimated from Zernike derivatives. The gain for the direct iterative feedback was set to 0.4 and the gain for the gradient feedback was set to 0.01. The combined control law outperformed the standard iterative modal feedback control law as seen in Figure 35, Figure 36, and Figure 37. The RMS wavefront error and peak to valley wavefront error is over three times smaller. The wavefront error also converges faster.

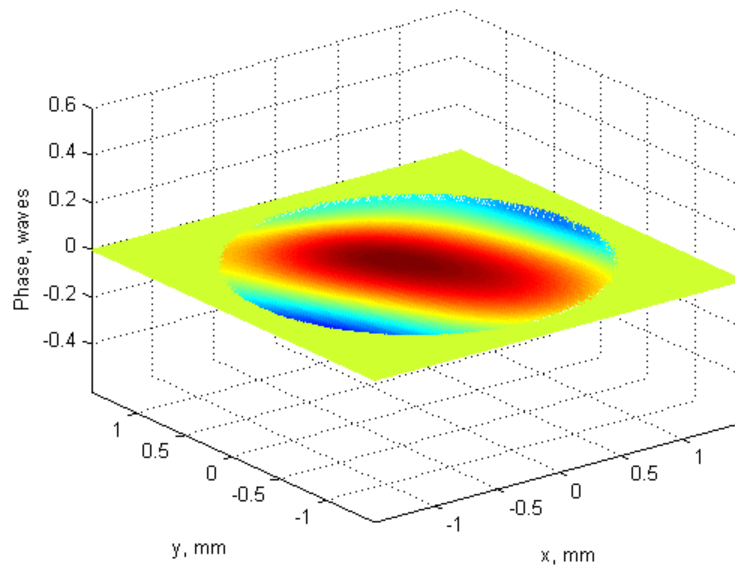


Figure 35 Corrected Wavefront Using Modal (derived from Zernike Derivatives)  
Iterative Feedback Control, Peak to Valley = 0.0788

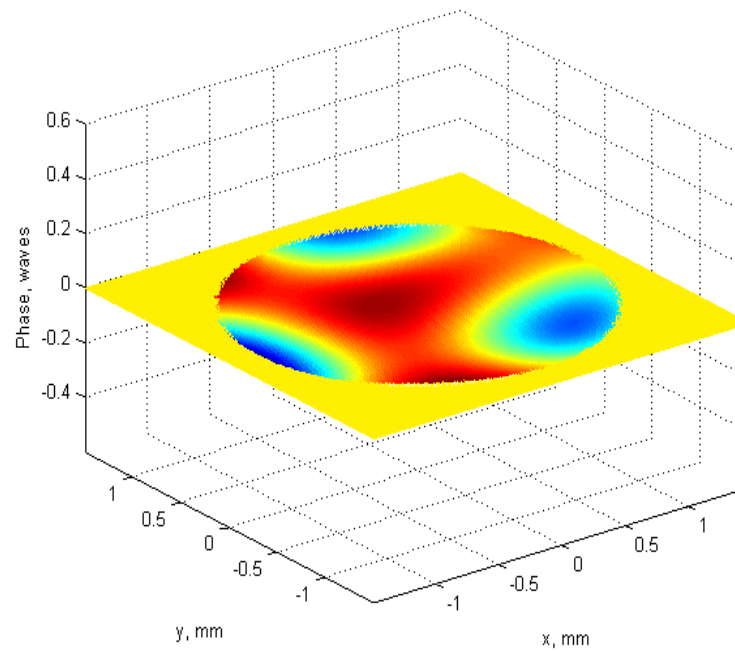


Figure 36 Corrected Wavefront Using Modal (derived from Zernike Derivatives)  
Iterative Feedback with Gradient Feedback Control, Multiple Gain, Peak  
to Valley = 0.0219

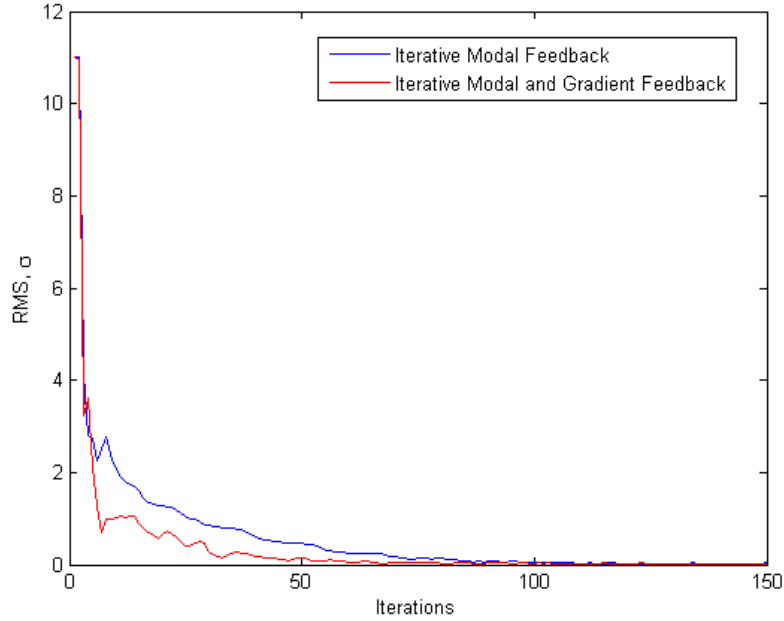


Figure 37 Error History Comparing Iterative Modal Feedback and Iterative Modal Feedback Combined with Gradient Feedback

## 5. Control Method Comparison

The wavefront estimation process of wavefront control makes up a large portion of the control loop. Although modal phase estimation adds an additional process to the wavefront control algorithm over an indirect method, it can also decrease the overall number of computations required per iteration. The number of numerical steps using modal phase estimation is dependent on the number of Zernike terms used to describe the wavefront. Therefore, it is possible to reduce the number of numerical computations in the control algorithm by using a modal phase estimation technique rather than using an indirect wavefront representation. Figure 38 shows the number of multiplication operations required for one iteration vs. the number of Zernike terms. The indirect method remains constant as it is dependent on the number of lenslets in the Hartmann mask, while the direct modal method is linearly dependent on the number of Zernike terms. In the previous experiments only 21 Zernike terms are used, therefore the direct modal iterative control algorithm has fewer multiplications than the indirect method

using slope information. However, if the number of Zernike terms is increased past 34 it is computationally beneficial to use a control algorithm with an indirect wavefront representation.

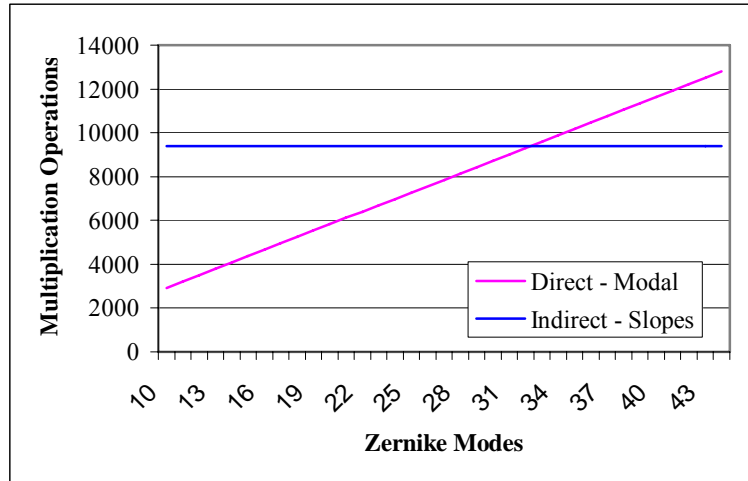


Figure 38 Multiplication Operations For Single Control Loop Iteration vs. Number of Zernike Modes Used, Using 37 Actuator Mirror, and 127 Lenslet Hartmann Mask, Modal Phase Representation from Zernike Derivatives, and Slope Representation from Measured x and y Slopes

Table 5 shows the error for the previously discussed control techniques. Analyzing the non-gradient iterative feedback control algorithms first, shows that the direct iterative feedback control using modal wavefront estimation from the Zernike derivatives performed the wavefront correction the best. The indirect iterative feedback controller using a singularity robust inverse also performed remarkably well. Both these techniques minimized the steps required to estimate the wavefront, or neglected a wavefront estimation altogether. Both techniques are singularity robust providing stability when inverting the influence matrix and computing the updated control signal. This accounts for their superior performance during the experiment.

Comparing the gradient approach, the slope minimization performed better than the variance minimization method. This is due to the variance minimization taking place over the continuous aperture using wavefront estimation while the slope minimization

process only takes place at the zonal phase points determined by the Hartmann mask. The slope minimization algorithm is likened to a finite element model, where the performance could be potentially improved by adding additional elements or lenslets over the aperture.

The best performance is achieved by combining the direct iterative feedback using modal phase estimation from Zernike derivatives with the gradient feedback method minimizing the variance. This method overcomes the inherent local minimum problem with gradient minimization approaches and also allows faster convergence by adaptively adjusting the control signal based on the rate at which the error is changing.

<b>Control Algorithm</b>	<b>Peak to Valley</b>	<b>RMS Wavefront Error</b>
Indirect Iterative Feedback SVD	5.424	2.819
Indirect Iterative Feedback SR	0.266	0.143
Direct Iterative Feedback, Zonal	6.092	2.383
Direct Iterative Feedback, Modal From Zonal	0.268	0.086
Direct Iterative Feedback, Modal from Zernike Derivatives	0.082	0.028
Iterative Gradient Feedback, Variance Minimization	0.736	0.199
Iterative Gradient Feedback, Slope Minimization	0.337	0.089
Combined Direct Iterative and Gradient Feedback	0.022	0.008

Table 5 Error Comparison for Wavefront Control Methods

### C. MMDM CORRECTION SUBJECT TO A DISTURBANCE

The next experiment subjects the MMDM to a low frequency sinusoidal disturbance. The disturbance is input into the mirror by adjusting the actuator control voltages. This experiment is conducted using the MMDM. A disturbance signal with a frequency of 5 Hz and amplitude of 54 was introduced to the mirror. The mirror is biased at 240 for the start of each experiment and the controller is operated for 250 iterations. Five of the control laws developed in the previous section were evaluated for their ability to correct a dynamic disturbance in the mirror.

The five control laws evaluated are the Indirect Iterative Feedback using a singularity robust inverse, direct iterative feedback using modal phase estimation from Zernike derivatives, the iterative gradient feedback using variance minimization, the iterative gradient feedback using slope minimization, and the combined iterative and

gradient feedback. Figure 40 through Figure 44 show the RMS wavefront error history for the five controllers with and without a disturbance. Figure 39 shows the error imparted on a planar wave when the mirror is subjected to the disturbance signal with no control resulting in a peak RMS wavefront error of 0.8546. The peak steady state RMS wavefront errors are used to compare the algorithms, Table 6. The gradient methods performed poorly adding additional error to the wavefront. The iterative feedback methods including the combined iterative feedback with gradient feedback method were all comparative in performance, driving down the wavefront error from the biased position but leaving residual error due to the disturbance signal. All the controllers could benefit from using notch filters to remove the known sinusoidal disturbance.

The poor performance of the gradient method is due to the bandwidth of the sensors and the control loop, approximately 30Hz. The control signal is computed based on the derivative of the error with respect to the control signal. This causes the controller to over correct adding additional error to the wavefront. Increasing the bandwidth of the sensor and the control loop would improve the iterative gradient controller performance, by decreasing the iterative step size. The additional error may also be reduced by decreasing the gain at the cost of increasing the settling time.

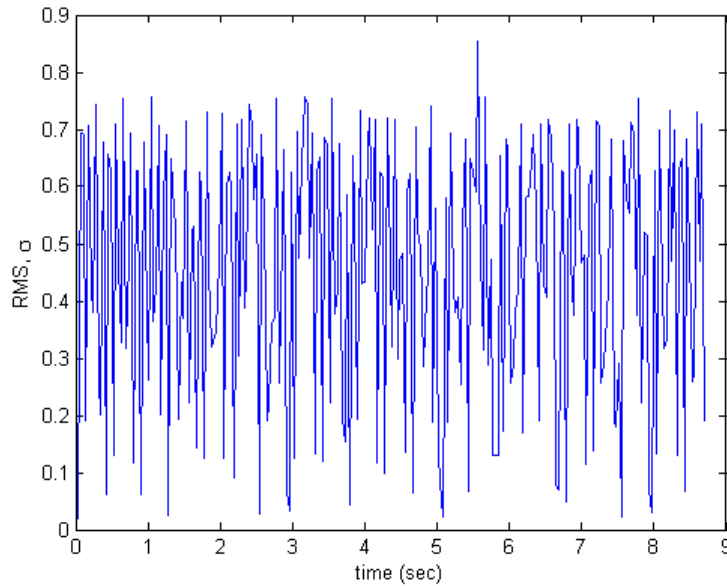


Figure 39 RMS Wavefront Error of Planar Surface Subjected to 5 Hz Sinusoidal Disturbance with Amplitude of 54 Volts

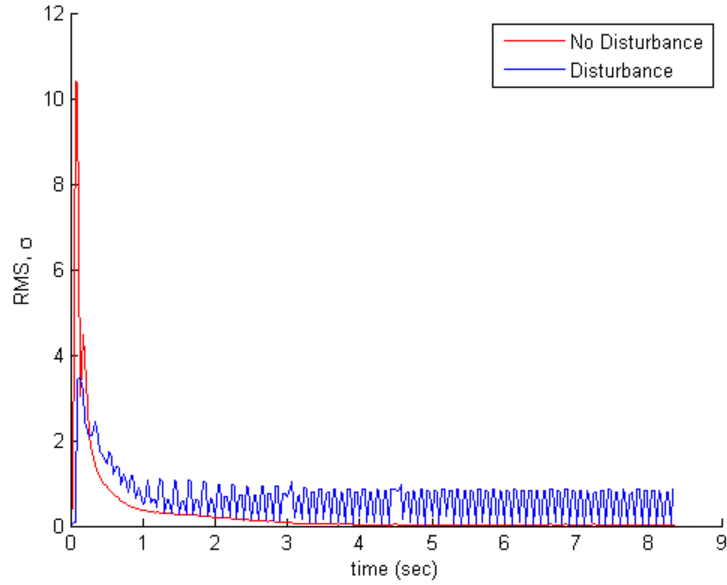


Figure 40 Error History Using Indirect Iterative Feedback with Singularity Robust Inverse, with and without 5 Hz Sinusoidal Disturbance

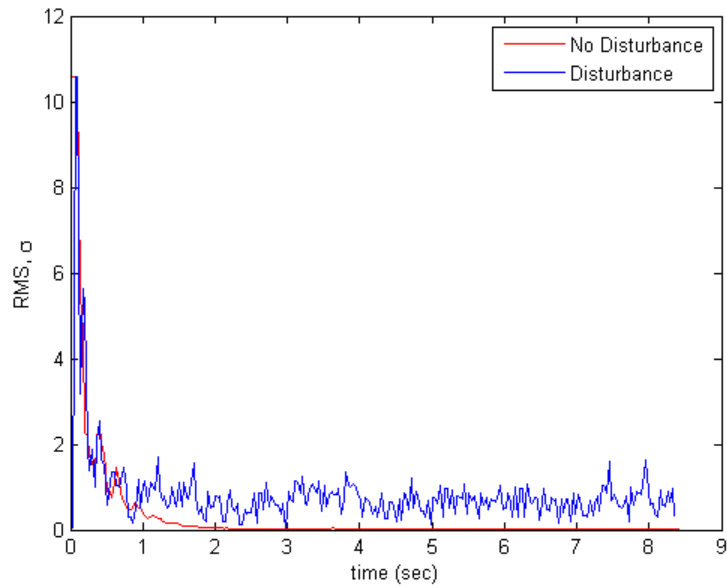


Figure 41 Error History Using Direct Iterative Feedback with Modal Phase Estimation from Zernike Derivatives, with and without 5 Hz Sinusoidal Disturbance



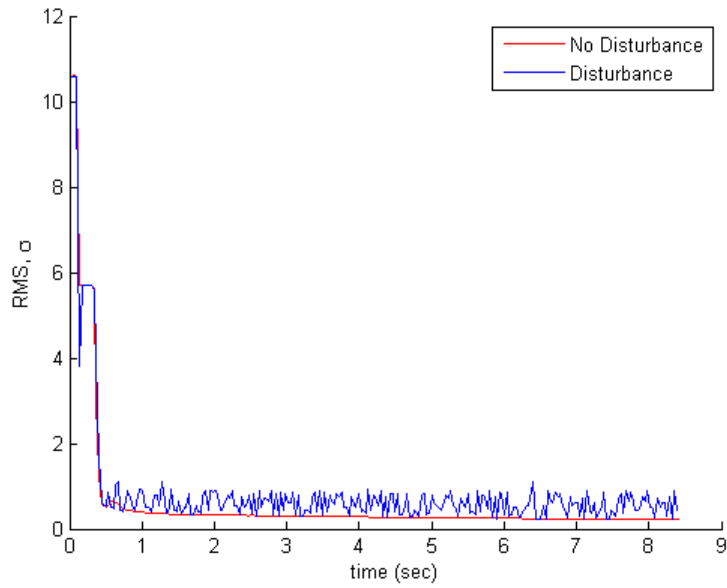


Figure 42 Error History Using Iterative Gradient Feedback Minimizing Variance, with and without 5 Hz Disturbance

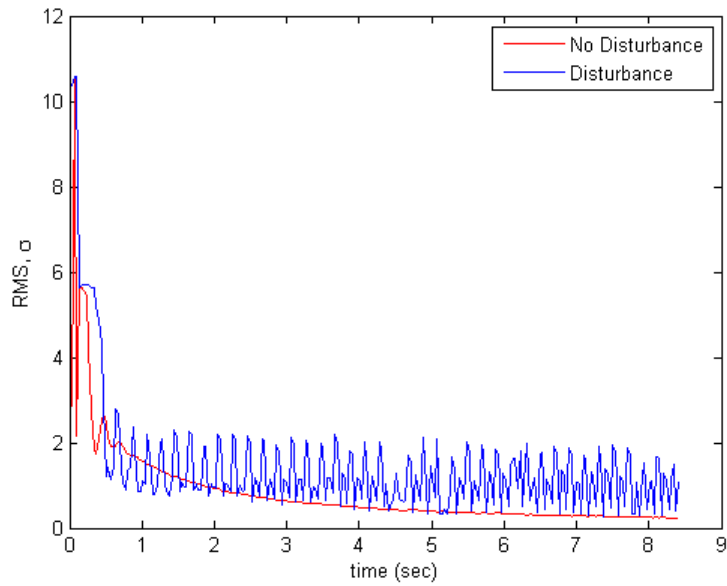


Figure 43 Error History Using Iterative Gradient Feedback Minimizing Slopes, with and without 5 Hz Disturbance

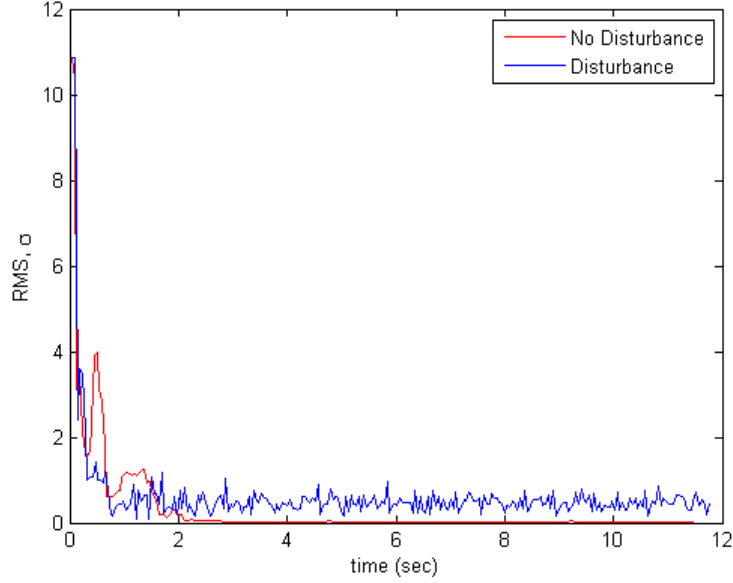


Figure 44 Error History Using Combined Direct Iterative and Gradient Feedback, with and without 5 Hz Sinusoidal Disturbance

	No Disturbance	Disturbance
<b>Control Method</b>	$\sigma$	$\sigma_{\max}$ at steady state
Indirect Iterative Feedback SR	0.0176	0.91261
Direct Iterative Feedback, Modal from Zernike Derivatives	0.2317	0.8897
Iterative Gradient Feedback, Variance Minimization	0.10174	1.95
Iterative Gradient Feedback, Slope Minimization	0.0288	1.6483
Combined Direct Iterative and Gradient Feedback	0.00619	0.8547

Table 6 Comparison of Control Methods Subject to a 5 Hz Sinusoidal Disturbance

## D. NOTCH FILTERING

### 1. Filtering Noisy Actuators

The discrete time notch filter is tested by introducing a sinusoidal disturbance to an individual actuator on the MMDM and applying the notch filter to the control law to remove the disturbance. A single actuator is tested first to minimize coupling between notch filters on multiple actuators. The notch filter was tested using the indirect iterative feedback control algorithm using a singularity robust inverse. This control algorithm was chosen to test the notch filter because the algorithm runs consistently faster than the

algorithms with modal phase estimation and performs comparably well. The control algorithm operates between 28 and 30 Hz. With this sampling rate the notch filter should be able to handle a low frequency sinusoidal disturbance less than 5 Hz.

*a. 5 Hz Sinusoidal Disturbance on Single Actuator*

The notch filter was tested against a 5 Hz sinusoidal disturbance with amplitude of 54. The notch filter was tuned to 5 Hz and a bandwidth of  $0.5\pi$ . Figure 45 shows the RMS error history for the surface of the wavefront with and without the notch filter. The notch filter reduced the sinusoidal disturbance and the maximum RMS error. Figure 46 shows the control history showing that the error signal is still present in the control signal, but at a significantly lower amplitude. The remaining error is due to uncertainties in the sampling rate changing the disturbance frequency. Increasing the bandwidth of the notch filter will improve performance by reducing the sinusoidal disturbance on the actuator, but will also reduce the control influence of the actuator.

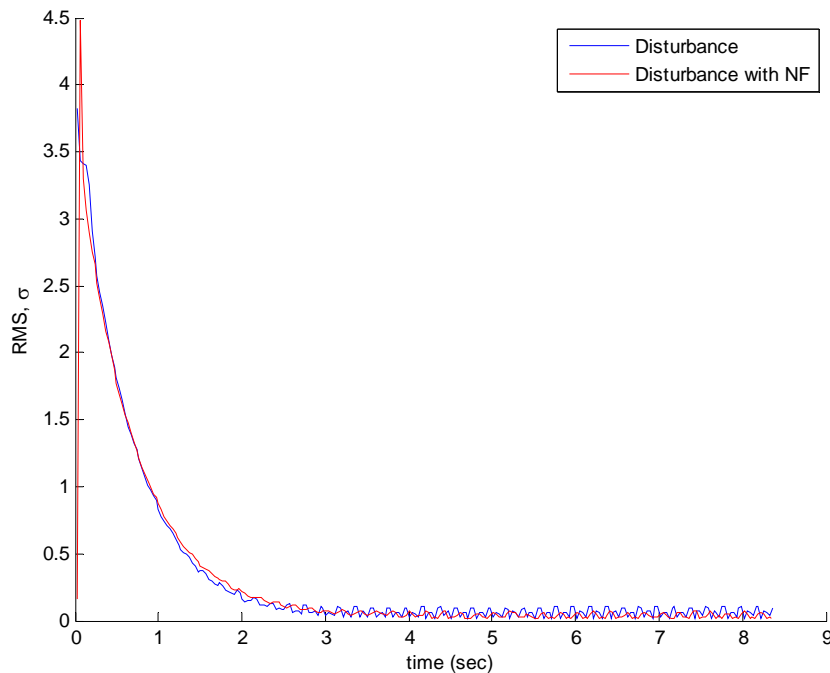


Figure 45 Error History for 5 Hz Sinusoidal Disturbance with an Amplitude 54 Volts, on MMDM Actuator 10, with and without Notch Filter, Initial Bias of 127

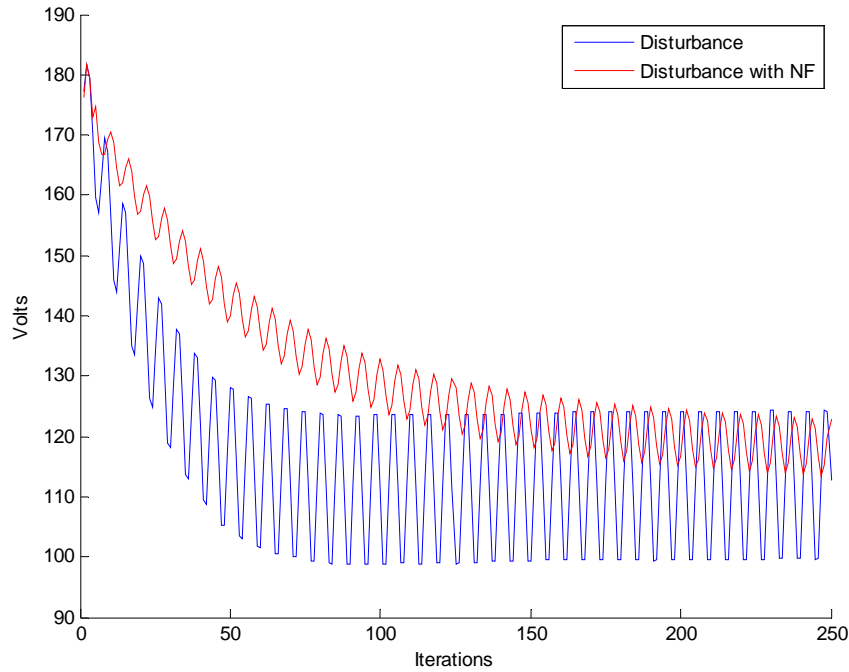


Figure 46 Control History for MMDM Actuator 10 with and without Notch Filter, 5 Hz Sinusoidal Disturbance, 54 Amplitude

***b. 2 Hz Sinusodial Disturbance on Single Actuator***

Using the same actuator but applying a 2 Hz sinusoidal disturbance the bandwidth of the notch filter is set to  $0.1\pi$  and  $0.5\pi$ . The error history, Figure 47, shows that the RMS wavefront error is improved by setting the notch filter to a higher bandwidth. The control history also shows a reduced sinusoidal disturbance in the control signal at the higher bandwidth, Figure 48. The wider bandwidth shows improvement because it also reduces the gain of adjacent frequencies, which helps account for the uncertainty in the sampling time of the computer control loop which adds uncertainty to the disturbance signal.

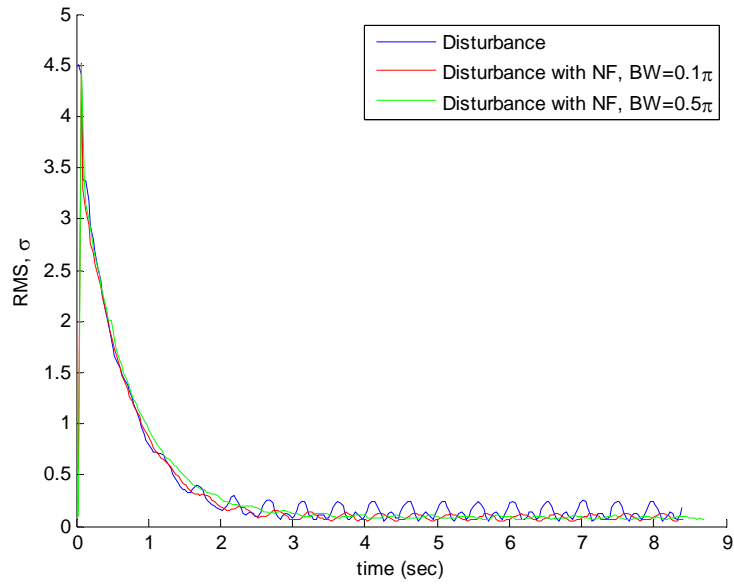


Figure 47 Error History for 2 Hz Sinusoidal Disturbance with an Amplitude 54 Volts, on MMDM Actuator 10, with and without Notch Filter, Initial Bias of 127

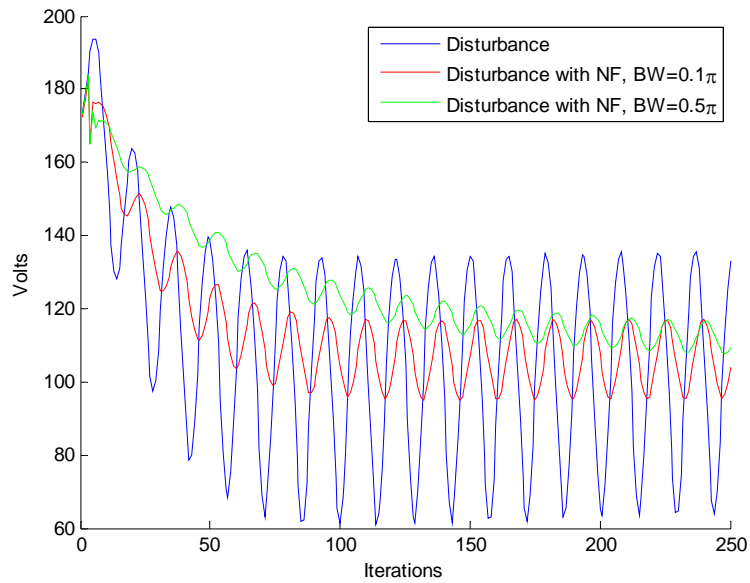


Figure 48 Control History for MMDM Channel 10 with and without Notch Filter, 2 Hz Sinusoidal Disturbance, 54 Amplitude

*c. Cascaded Notch Filters on Single Actuator*

Two disturbances at different frequencies were introduced into actuator 10 and a cascading notch filter was applied to remove the disturbance. The cascading notch filters were set to 0.8 Hz and 2 Hz respectively with a  $0.5\pi$  bandwidth and successfully reduced the RMS wavefront error. A residual disturbance is still evident in both the error and control history seen in Figure 49 and Figure 50. The overall RMS wavefront error is greater than the previous experiments where only one disturbance frequency was introduced. This is partially due to the overall gain drop at adjacent frequencies as seen in the Bode plot, Figure 20.

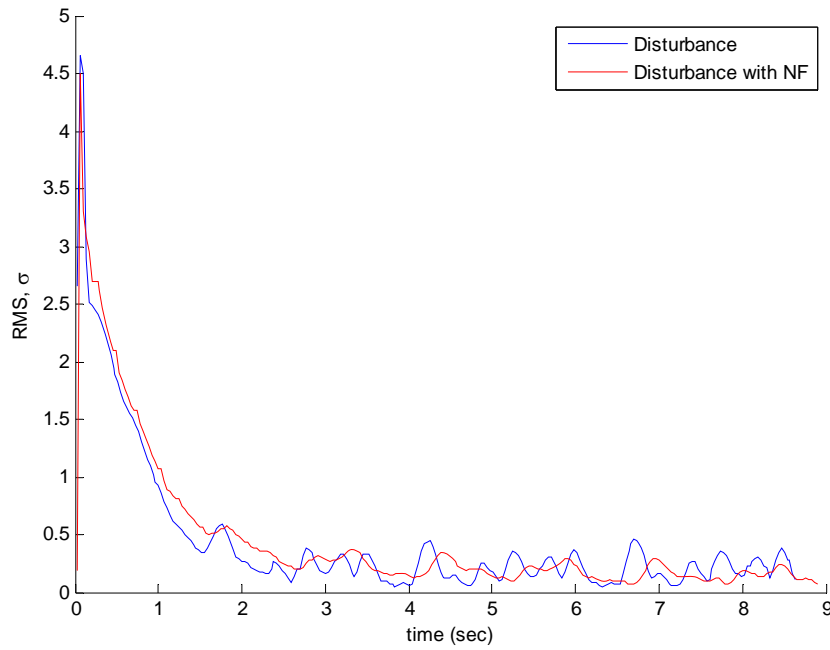


Figure 49 Error History for .08 and 2 Hz Sinusoidal Disturbance with an Amplitude 54 Volts, on MMDM Actuator 10, with and without Cascading Notch Filter, Initial Bias of 127

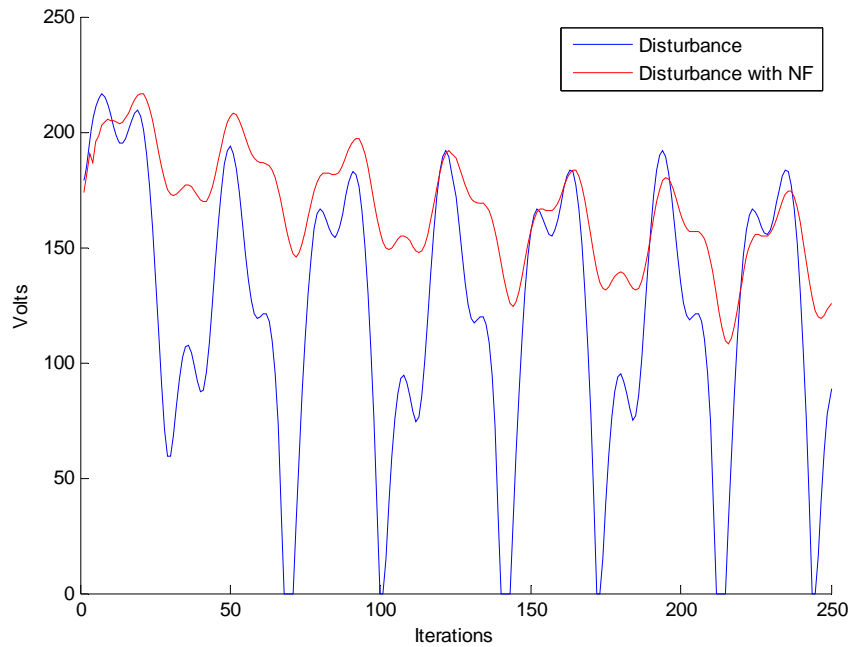


Figure 50 Control History for MMDM Channel 10 with and without Cascading Notch Filter, 0.8 and 2 Hz Sinusoidal Disturbance, 54 Amplitude

***d. 2 Hz and 0.8 Hz Sinusoidal Disturbance on Non-Adjacent Actuators***

A second disturbance was added to the mirror at actuator 16. Actuators 10 and 16 are on opposite sides of the face sheet to minimize coupling. Both actuators were subjected to a sinusoidal disturbance with two different frequencies, 2 Hz on actuator 10 and 0.8 Hz on actuator 16. The notch filters were tuned to 2.0 and 0.8 Hz respectfully and a bandwidth of  $0.5\pi$ . The notch filters performed well reducing the overall RMS wavefront error, and removing the sinusoidal disturbance, as shown in Figure 51. The amplitude of the disturbance is reduced in both control signals with the higher frequency disturbance being reduced more than the lower frequency disturbance, as shown in Figure 52.

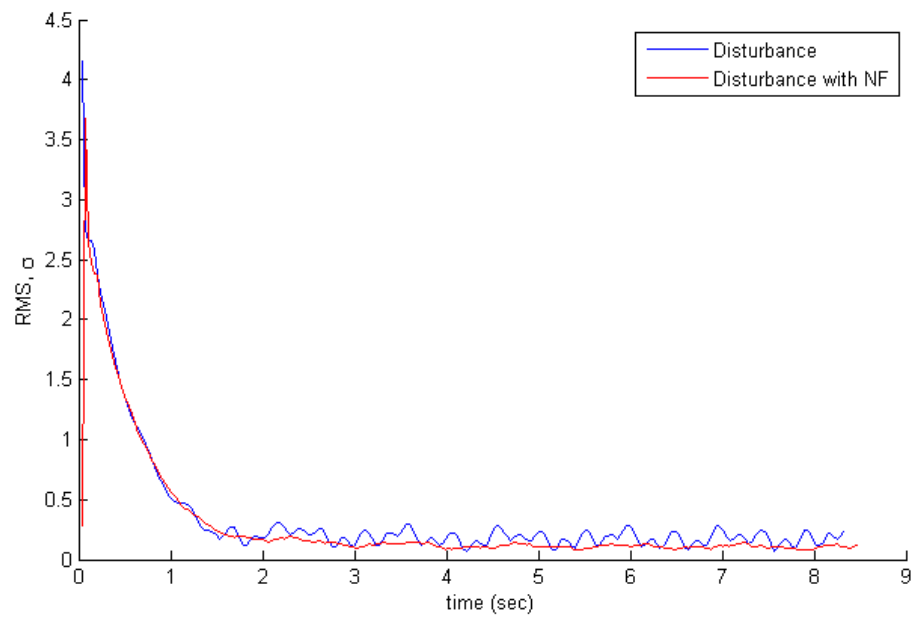


Figure 51 Error History for 2.0 Hz and 0.8 Hz Sinusoidal Disturbance with an Amplitude 54 Volts, on MMDM Actuator 10 and 16, with and without Notch Filter, Initial Bias of 127

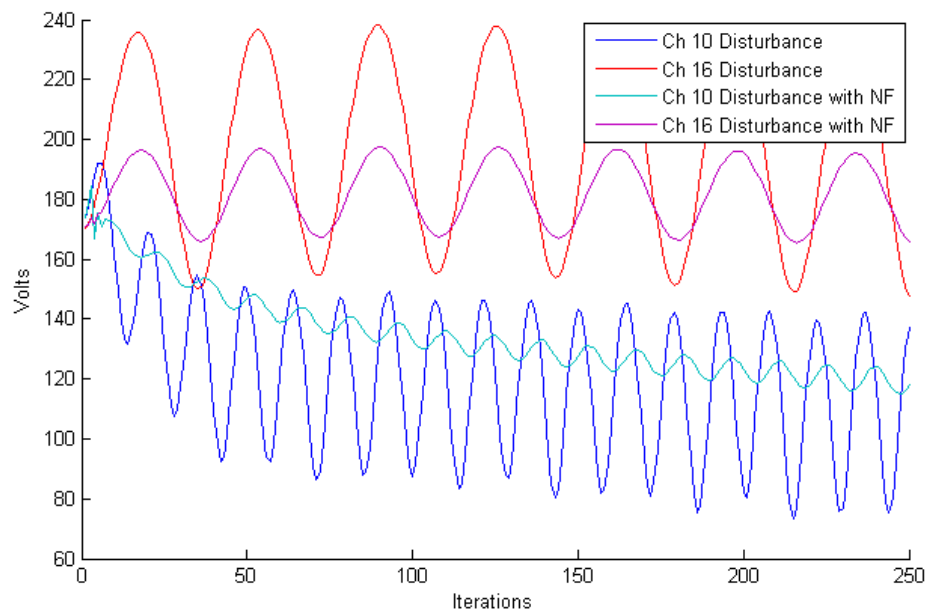


Figure 52 Control History for MMDM Channel 10 and 16 with and without Notch Filter, 2 Hz Sinusoidal Disturbance on Channel 10 and 0.8 Hz on Channel 16 with an Amplitude 54



*e. 2 Hz and 0.8 Hz Sinusoidal Disturbance on Adjacent Actuators*

To explore the coupling between actuator influences on the face sheet two disturbances were introduced to two adjacent actuators, 10 and 11. The same frequency disturbance is introduced on both actuators but with only one notch filter on actuator 10. The overall RMS wavefront error was decreased; however, a residual error is still present at 2 Hz due to the error caused by actuator 11, as shown in Figure 53. The control signal history of actuator 10 shows that the disturbance was successfully decreased while the control history for actuator 11 shows a decrease in the maximum control voltage, but similar absolute amplitude at steady state. The change in control voltage demonstrates the coupling of the actuators due to the continuous surface of the face sheet.

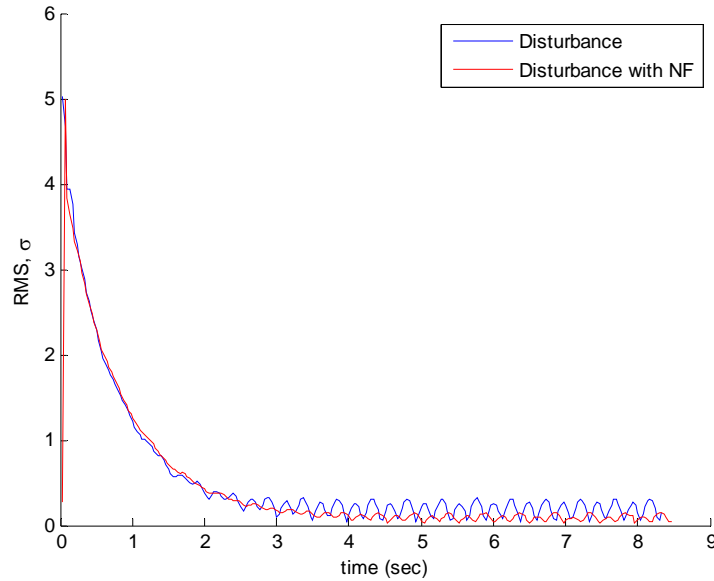


Figure 53 Error History for 2.0 Hz Sinusoidal Disturbance with an Amplitude 54 Volts, on MMDM Actuator 10 and 11, with and without Notch Filter, Initial Bias of 127

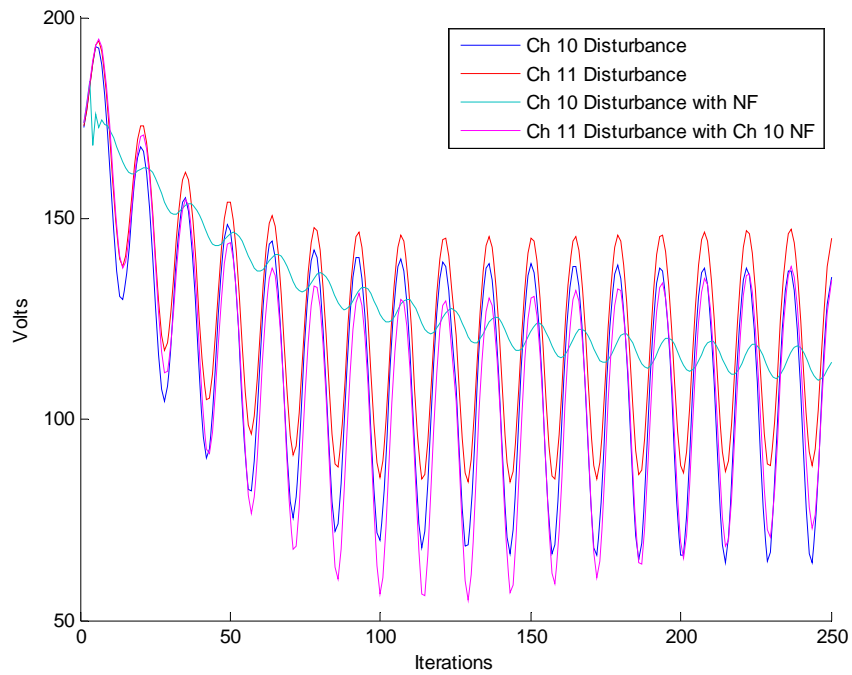


Figure 54 Control History for MMDM Channel 10 and 11 with and without Notch Filter, 2 Hz Sinusoidal Disturbance on Channel 10 and Channel 11 with an Amplitude 54

A similar experiment to the previous is conducted using two different frequency disturbances on the two separate actuators, 10 and 11, with a notch filter only on actuator 10. The results are similar to the previous results with the higher frequency disturbance being removed from actuator 10 and the lower frequency disturbance present in both the error and control history plots due to actuator 11, as shown in Figure 55 and Figure 56. Again, the adjacent notch filter impacts the control signal of actuator 11 when implemented with the control law.

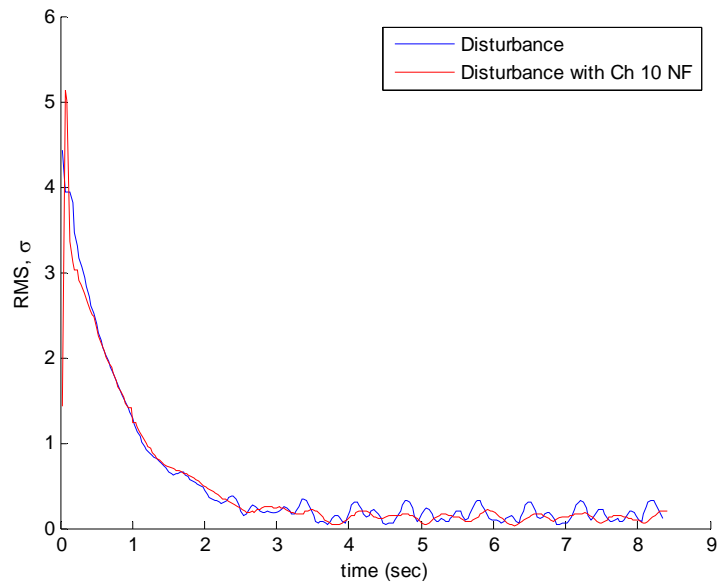


Figure 55 Error History for 2.0 Hz and 0.8 Hz Sinusoidal Disturbance with an Amplitude 54 Volts, on MMDM Actuator 10 and 11, with and without Notch Filter on Actuator 10, Initial Bias of 127

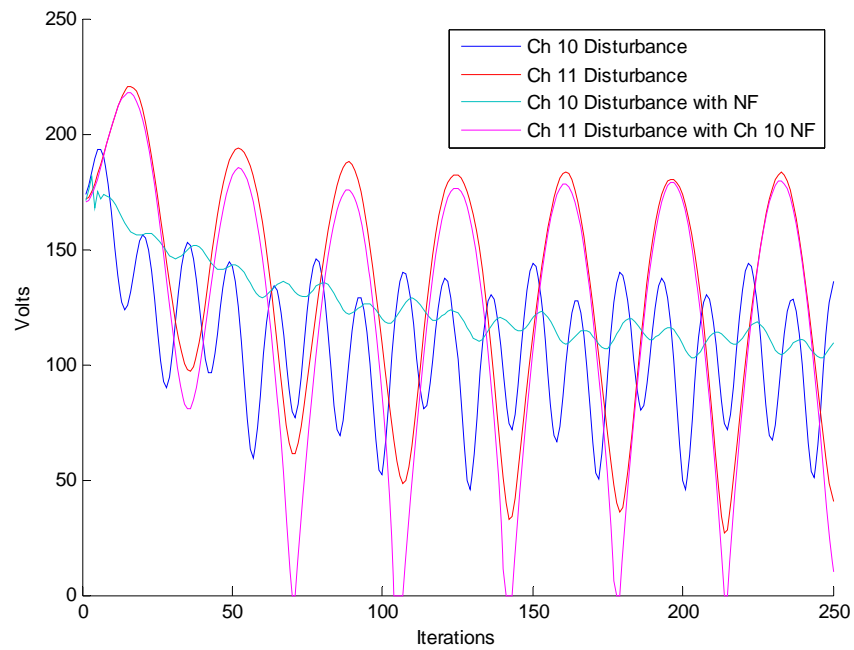


Figure 56 Control History for MMDM Channel 10 and 11 with and without Notch Filter, 2 Hz and 0.8 Hz Sinusoidal Disturbance on Channel 10 and Channel 11 with an Amplitude 54

Two notch filters were applied to the adjacent actuators, 10 and 11. The notch filters were tuned to the appropriate frequencies with a bandwidth of  $0.5\pi$ . The results show that the disturbance is notched out successfully reducing the RMS wavefront error. The error is reduced by a factor of four over using just the iterative control law alone. The improved RMS wavefront error over the previous experiment where a non-adjacent actuator was used is due to the localization of the disturbance on the face sheet.

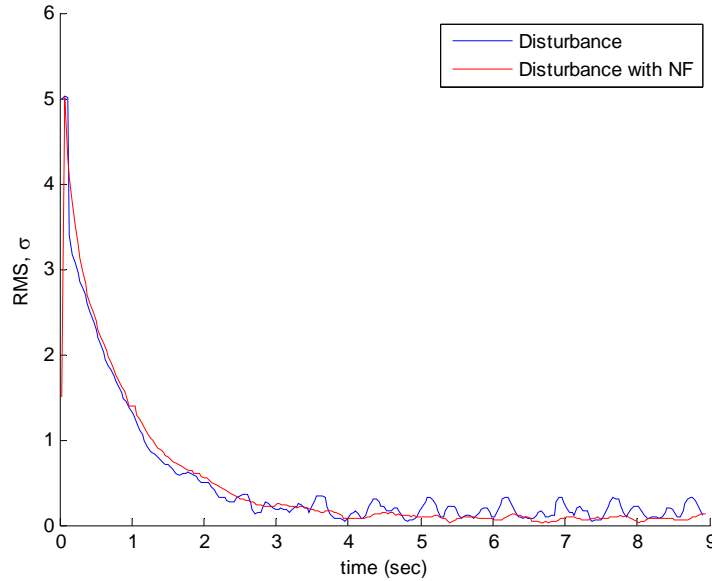


Figure 57 Error History for 2.0 Hz and 0.8 Hz Sinusoidal Disturbance with an Amplitude 54 Volts, on MMDM Actuator 10 and 11, with and without Notch Filter, Initial Bias of 127

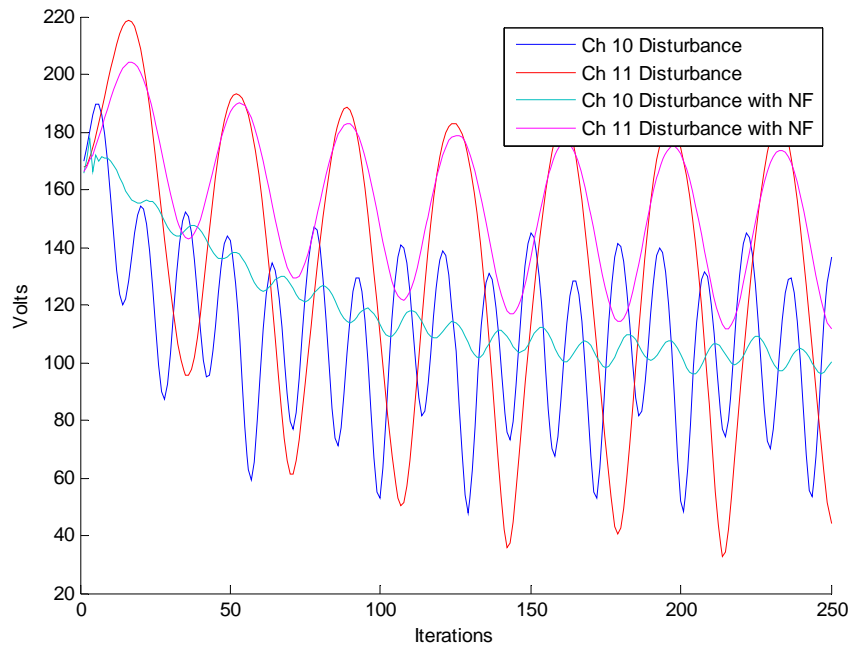


Figure 58 Control History for MMDM Channel 10 and 11 with and without Notch Filter, 2 Hz Sinusoidal Disturbance on Channel 10 and 0.85 Hz on Channel 11 with an Amplitude 54

*f. 2 Hz Sinusoidal Disturbance on 37 MMDM Actuators*

In this experiment, a 2 Hz sinusoidal disturbance and a discrete time notch filter are applied to all the actuators. The filter bandwidth is set to  $0.1\pi$ . The notch filter performed well reducing the maximum steady state wavefront disturbance by a factor of four. The narrow bandwidth of the notch filter allows for a quick settling time but allows some of the disturbance to pass due to the uncertainty of the disturbance frequency. Increasing the bandwidth will decrease the overall error but will also increase the settling time by reducing the overall actuator gains.

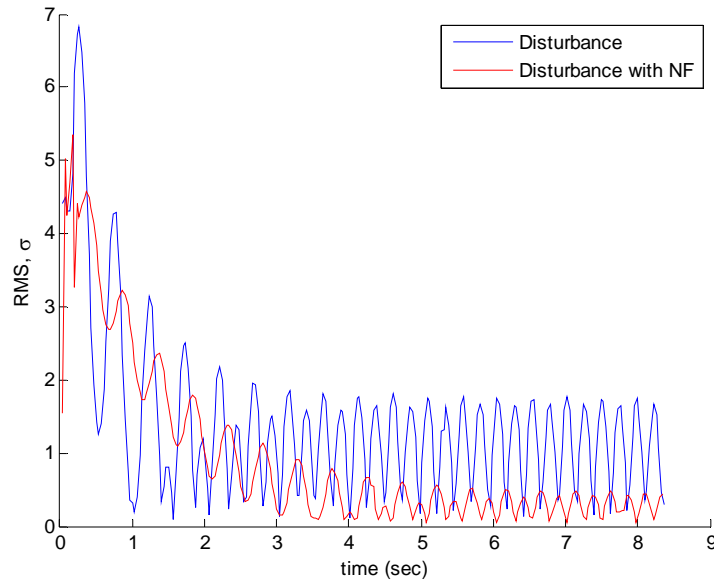


Figure 59 Error History for 2.0 Hz Sinusoidal Disturbance with an Amplitude 54 Volts, on 37 MMDM Actuators, with and without Notch Filter, Initial Bias of 127

## 2. Filtering a Simulated Vibration

A simulated disturbance due to vibration is introduced into the MMDM using the previously discussed modal iterative feedback control law using wavefront estimation from Zernike derivatives. A disturbance is introduced into the mirror by introducing a sinusoidal disturbance into the third Zernike term, which represents focus. This creates an oscillating focus aberration on the surface of the mirror and in the wavefront. The disturbance simulates a first mode vibration disturbance across the face sheet at a specific frequency. Unlike the previous notch filter experiment where each actuator had the same disturbance signal, the actuator voltages are adjusted to achieve the desired wavefront and mirror aberration. The second order notch filtering techniques previously developed are applied to the modal iterative feedback control law to reduce the disturbance.

The resulting error history for the disturbance shows that the notch filter was able to remove a portion of the disturbance successfully using a bandwidth of  $0.2\pi$ , Figure 60. However by increasing the bandwidth to  $0.8\pi$  the notch filter was able to almost

completely remove the simulated structural disturbance across the face sheet. The resulting steady state RMS wavefront error is comparable to the corrected wavefront results achieved without a disturbance but at the cost of a greater settling time, Figure 61.

The filters only operate well if the frequency of the disturbance is known exactly, as seen in all the notch filter experiments. The uncertainty in sampling time of the experimental testbed prevented the notch filters from performing exactly as designed. Despite the filters not being tuned exactly they all reduced the disturbance regardless if the disturbance signal represented actuator, sensor, or structural disturbance. The experimental notch filtering results shown in Table 7 show that the higher bandwidth filters tend to perform better. However, a wider bandwidth filter may have some consequences in a non-laboratory system, where adjacent frequency information may be desired.

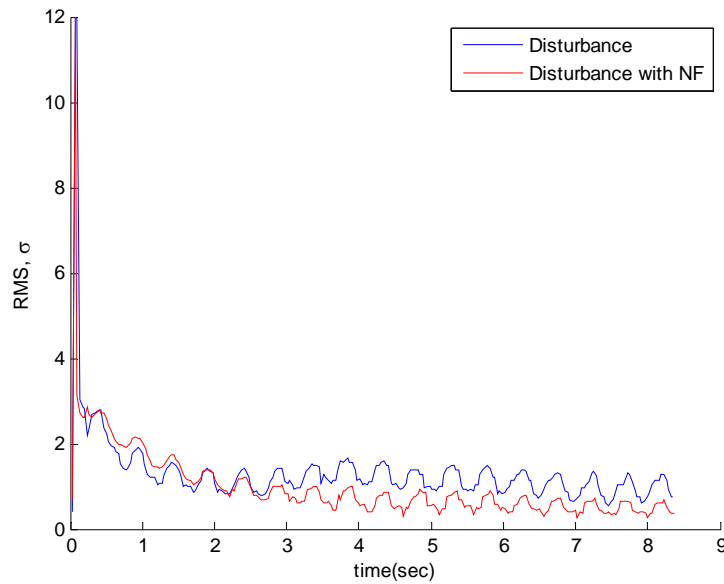


Figure 60 Error History for 2.0 Hz Sinusoidal Disturbance on Wavefront Focus, with and without Notch Filter, Bandwidth =  $0.2\pi$ , Initial Bias of 127

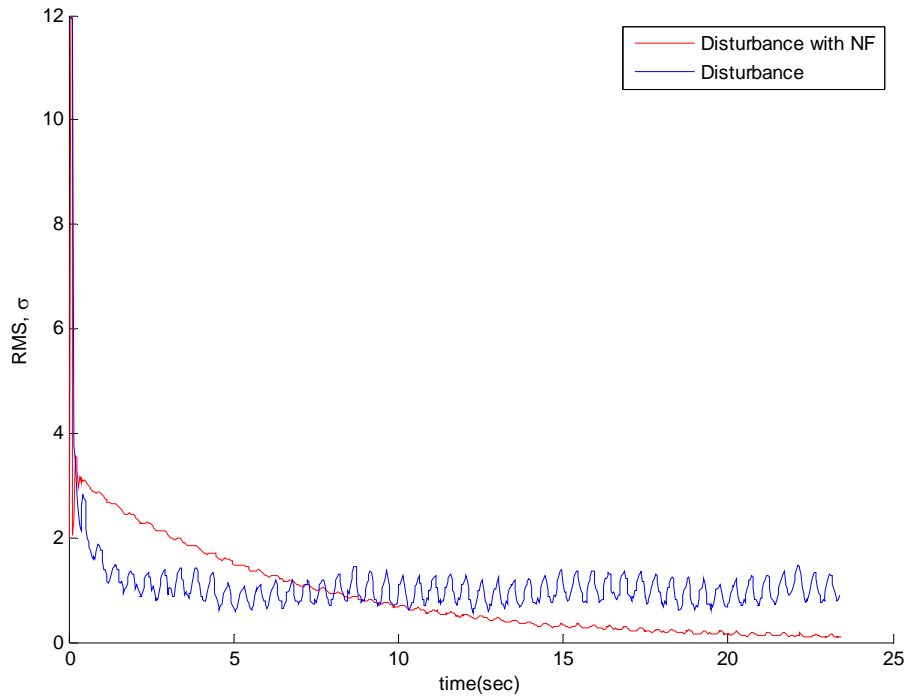


Figure 61 Error History for 2.0 Hz Sinusoidal Disturbance on Wavefront Focus, with and without Notch Filter, Bandwidth =  $0.8\pi$ , Initial Bias of 127

Channel	Frequency (Hz)	Bandwidth of NF	$\sigma$ without Filtering	$\sigma$ with Filtering
10	5	$0.5\pi$	0.105	0.074
10	2	$0.1\pi$	0.224	0.104
10	2	$0.5\pi$	0.224	0.075
10	2 and 0.8	$0.5\pi$	0.465	0.291
10 and 16	2 and 0.8	$0.5\pi$	0.2185	0.085
10 and 11 (NF on 10)	2	$0.5\pi$	0.312	0.151
10 and 11 (NF on 10)	2 and 0.8	$0.5\pi$	0.329	0.208
10 and 11	2 and 0.8	$0.5\pi$	0.327	0.134
All	2	$0.1\pi$	1.778	0.483
Simulated Vibration	2	$0.2\pi$	1.47	0.708
Simulated Vibration	2	$0.8\pi$	1.47	0.0405

Table 7 Notch Filtering RMS Wavefront Error Comparison



## **VII. SUMMARY, CONCLUSIONS, AND FUTURE WORK**

### **A. SUMMARY**

In order to experimentally validate current technology and develop new wavefront control techniques for future space telescopes, an adaptive optics testbed was designed and built at the Spacecraft Research and Design Center, Naval Postgraduate School. This testbed is unique in its ability to experimentally test control algorithms for both jitter and wavefront control. This research used the adaptive optics testbed to demonstrate wavefront control techniques for correcting a deformable mirror and rejecting known disturbances introduced into the mirror.

Wavefront estimation and representation techniques were investigated and evaluated when combined with an iterative feedback control algorithm. The control algorithms were evaluated by comparing the steady state RMS wavefront error and peak to valley wavefront error by correcting the wavefront from a biased position. The control algorithms were then evaluated subject to a 5 Hz sinusoidal disturbance on the actuators and evaluated. Notch filtering techniques were also investigated, with known sinusoidal disturbances at 0.8 Hz and 2 Hz introduced as actuator noise and as a simulated structural disturbance. The notch filter was combined with both a direct and indirect iterative feedback controller and the RMS wavefront error was compared.

### **B. CONCLUSION**

This research has shown that the direct modal wavefront estimation techniques outperformed the indirect wavefront representation techniques when combined with the iterative feedback control laws. The indirect wavefront control methods could be improved by using a singularity robust inverse technique when inverting the influence matrix; however, the direct modal wavefront control techniques still provided superior performance.

The experimental results also showed that a combination of an iterative feedback and gradient feedback control law using variance minimization provided the smallest

RMS wavefront error when correcting from a biased position and when correcting the mirror subjected to a sinusoidal noise disturbance. However, the combined controller is very sensitive to the gains, requiring both the iterative gain and the gradient feedback gain to be properly tuned. All the control algorithms showed a residual disturbance in the wavefront error when subjected to a sinusoidal disturbance.

The experimental results demonstrated that a second order discrete time notch filter can be used in the adaptive optics control algorithm to improve the steady state RMS wavefront error when a known constant frequency disturbance is present. Applying a properly tuned notch filter in series with either a direct or indirect controller decreased or removed the dynamic disturbance. The notch filter success in the experimental work was dependent on knowledge of the disturbance frequency, the notch filter bandwidth, and the knowledge of the computer sampling time. The experimental work successfully demonstrated that low frequency filtering of actuator noise as well as a simulated structural disturbance, achieving a wavefront error comparable to results achieved without a disturbance.

### **C. FUTURE WORK**

The current testbed and future research can be improved by upgrading the wavefront sensors. The current sensors are too slow to observe the dynamics of the mirrors, or higher frequency disturbances. Increasing the wavefront sensor speed will be an immediate improvement to current and future control algorithms.

Although the control algorithms worked well on the current testbed the current mirrors do not have the dynamics of a large light weight mirror. Future research should be conducted using a larger light weight flexible mirror with lower structural resonant frequencies. This will require robust control techniques and adaptive filtering techniques to control the system when the disturbance is not known precisely, and to account for uncertainty in the system. Additionally the control techniques developed in this thesis could be compared with multi-input and multi-output control techniques that incorporate

the structural dynamics of the mirror. In addition to face sheet control as discussed in this paper, particular attention should be given to segmented mirror control, as future space telescopes will most likely be segmented.

The SRDC in cooperation with the Naval Research Labs has purchased an 16 inch diameter light weight six segment mirror. This mirror will allow future research into control techniques to properly align and phase the mirror segments. In addition to the new mirror, new phase diversity sensors will also be included in the experimental testbed. Eventually the control algorithms discussed in this research may be combined and adapted to be used with the segmented mirror control algorithms to control a segmented mirror with deformable face sheets.

THIS PAGE INTENTIONALLY LEFT BLANK

## APPENDIX A. SOFTWARE VERSIONS

Software	Version	Function
MATLAB	R2007a	Interface Computer with MMDM, PDM
MATLAB	R2006a	Interface Computer with DSPACE
DSPACE	R5.1	Interface Computer to FSM
Windows XP	Profession Version 2002, SP2	Control Computer Operating System

Table 8    Software Versions

THIS PAGE INTENTIONALLY LEFT BLANK

## APPENDIX B. SAMPLE MATLAB CODE

### A. INITIALIZATION

```
%-----
%Matt Allen                                October 5, 2007
%Iterative_method.m
%This script uses Zernike Polynomials for wavefront estimation. This
%script is used to initialize the control algorithm by computing the
%influence matrix (poke matrix).
%-----
clc;
clear all;
close all;

%-----
%Define Constants
%-----

pw=.009630;           %pixel width in mm
fl=17.361408;        %focal length in mm
w2=wk;               %Weighting Factors for Zernike Polynomials (Variance)

%-----
%Load and process Reference Image - Calibrate
%-----

TH=150;               %Threshold for CCD
I=imread('Calibrate.bmp'); %Read in calibrated reference image
I(1:20,304:324)=0;    %Block Out Extra Pixel
[Grid Ref_init]=Ref_Grid_init(I,TH); %Compute Reference Grid
Locations
s_grid=Grid;
%Reference_Grid=round(s_grid); %Round Reference Grid to nearest pixel
offset_x=s_grid(64,1);
offset_y=s_grid(64,2);
s_grid(:,1)=s_grid(:,1)-offset_x; %Center Reference Grid x=64
s_grid(:,2)=s_grid(:,2)-offset_y; %Center Reference Grid y=64
Ref=s_grid;

%-----
%Build Influence (Poke) Matrix
%-----
for i=1:37             %Loop based on Number of Actuators

    V=ones(1,37)*sqrt(.5)*240; %create a voltage settings vector
    V(i)=240;
    BAODMirror(hex2dec('C800'),hex2dec('CC00'),V);
    pause(.1)             %Delay Required to Command Mirror
    BAOGrab(0);           %initialize
```

```

        SH=(BAOGrab(1))';           %grab images from the Shack-Hartmann
WFS
        BAOGrab(2);                 %de-initialize mirror

        SH(1:20,304:324)=0;         %Blockout extra lenslet
        Data=Process_Image(SH,Ref_init); %Compute Centroids, pass image,
and thresh hold
        Data(:,1)=Data(:,1)-offset_x;
        Data(:,2)=Data(:,2)-offset_y;
        Zs(:,i)=reshape(Data,254,1);

end

%-----
%Estimate Wavefront of Poke Matrix Using Zernike Polynomials (21 terms)
%return Influence matrix of Zernike Coefficients
%-----

B=Bmatrix(Zs,Ref);                 %Builds Modal Influence Matrix

```

## B. WAVEFRONT SENSOR PROCESSING

```

%-----
%Matt Allen                               Aug 18,2007
%Process_Image.m
%This function is used in conjunction with the program Ref_Grid_init.m
%This function reads in the reference lenslet location 'Ref_init'
%computed
%from the function 'Ref_Grid_init.m'and sections out the lenslet array
%areas in the image 'SH'. A centroid is then computed and returned as
%the vector 'Grid'.
%-----
function Grid = Process_Image(I,Ref_init)

%Search Sub-Image
for i=1:127
    P=double(I(Ref_init(i,2)-10:Ref_init(i,2)+10,Ref_init(i,1)-
10:Ref_init(i,1)+10)); %Section out Lenslet
    S=size(P); S=S(1);
    M=(sum(sum(P))); %Compute Centroid
    X=(linspace(1,S,S))';
    Rx=P*X;
    Ry=X'*P;
    Rx=sum(Rx)*1/M;
    Ry=sum(Ry)*1/M;

    Grid(i,1)=Rx-10+Ref_init(i,1);
    Grid(i,2)=Ry-10+Ref_init(i,2); %X and Y Locations of
Reference Grid
end

```



## C. CONTROL ALGORITHM

```
%-----
%Matt Allen                                     31 October 2007
%Control_Law.m
%
%Apply Control Law Using Iterative Voltage Updating  $V_{n+1}=V_n-g\text{Binv}(S)$ ,
%where  $S$  is the slope measurement. This algorithm minimizes the slope
%difference as directly measured from the Shack-Hartmann Wavefront
%Sensor. The algorithm drives measured pixels to a reference pixel
%associated with a planar wavefront. This script requires the
%initialization script Iterative_method.m, and a reference image of a
%planar wavefront (or desired wavefront) named Calibrate.bmp
%-----
clear Error
clear Freq

s=reshape(Ref,254,1);
    BAOGrab(0);           %initialize
    SH=(BAOGrab(1))';     %grab image from Shack-Hartmann'
    BAOGrab(2);

    SH(1:20,304:324)=0;    %Block out extra lenslet
    Data=Process_Image(SH,Ref_init);
    Data(:,1)=Data(:,1)-offset_x;
    Data(:,2)=Data(:,2)-offset_y;
    Data=reshape(Data,254,1); %SH Location Data

    S1=Data-s;             %Compute the Slope

g=.01;

Binv=pinv(B);

cold=Binv*(S1);
tic;
for i=1:150

    BAOGrab(0);           %initialize
    SH=(BAOGrab(1))';     %grab image from Shack-Hartmann'
    BAOGrab(2);

    SH(1:20,304:324)=0;    %Block out extra lenslet
    Data=Process_Image(SH,Ref_init);
    Data(:,1)=Data(:,1)-offset_x;
    Data(:,2)=Data(:,2)-offset_y;
    Data=reshape(Data,254,1); %SH Location Data

    S1=Data-s;             %Compute the Slope

    cnew=cold-g*Binv*(S1);
        for p=1:37
            if cnew(p)<-1
```

```

        cnew(p)=-1;
        else if cnew(p)>1
            cnew(p)=1;
        end
    end
end
V=sqrt((cnew+1)*.5)*240;
cold=cnew;

BAODMirror(hex2dec('C800'),hex2dec('CC00'),V');
pause(.03)
end

```

## LIST OF REFERENCES

- Chen, C. T. (1993). Analog and digital control system design: transfer-function, state space, and algebraic methods (pp. 495-503). London: Saunders College Publishing.
- Frazier, B. W., & Tyson, R. K. (2002). Robust control of an adaptive optics system. *Proceedings of the Thirty-Fourth Southeastern Symposium on System Theory*, 293-296.
- Hsue, C. W., Chen, Y. J., & Tsai, Y. H. (2007, May). Design of bandstop filters using discrete time notch filter, two-section stub, and frequency-scaling method. *Microwave and Optical Technology Letters*, 49, 1098-1101.
- Industrial Vision Source. (2004, October). Miniature 1/3" or 1/2" monochrome machine vision cameras [Brochure]. Farmers Branch, TX. Retrieved November 6, 2007, from [http://www.i-v-s.com/data/pdfs/bwcam\\_ex\\_series.pdf](http://www.i-v-s.com/data/pdfs/bwcam_ex_series.pdf).
- JDS Uniphase. (2007). Helium-Neon laser heads 1100 series [Brochure]. Milpitas, CA. Retrieved November 17, 2007, from [http://products.jdsu.com/assets/public/pdf/hnlh1100\\_ds\\_cl\\_ae\\_012506.pdf](http://products.jdsu.com/assets/public/pdf/hnlh1100_ds_cl_ae_012506.pdf).
- Mathworks. (2007). Introduction to MEX-files. Retrieved November 6, 2007, from <http://www.mathworks.com/support/tech-notes/1600/1605.html#intro>.
- On-Trak Photonics Inc. (2005). Position sensing modules for non-contact measurement of: position, motion, distance, and vibration [Brochure]. Lake Forest, CA. Retrieved November 10, 2007, from <http://www.on-trak.com/pdfs/PSM.pdf>.
- Pie, S. C., & Tseng T. T. (1997). IIR multiple notch filter design based on allpass filter. *IEEE Transactions on Circuits and Systems II: Analog and Digital Signal Processing*. 44(2), 133-136.
- Southwell, W. H. (1980, August). Wave-front estimation from wave-front slope measurements. *Journal of the Optical Society of America*, 70(8), 998-1006.
- Tyson, R. K. (1998). Principles of adaptive optics (2nd ed.). San Diego, CA. Academic Press.
- Tyson, R. K. (2000). Adaptive optics engineering handbook. New York. Marcel Dekker, Inc.
- Wie, B. (2001, October). Singularity robust steering logic for redundant single-gimbal control moment gyros. *Journal of Guidance, Control, and Dynamics*, 25(5), 865-872.

- Wyant, J. C. (2003). Zernike polynomials for the web. Retrieved October 1, 2007, from The University of Arizona, College of Optical Sciences Web site:  
[www.optics.arizona.edu/jcwyant/Zernikes/ZernikePolynomialsForTheWeb.pdf](http://www.optics.arizona.edu/jcwyant/Zernikes/ZernikePolynomialsForTheWeb.pdf).
- Zhu, L., Sun, P.C., Bartsch, D. U., Freeman, W. R., & Fainman, Y. (1999, January). Adaptive control of a micromachined continuous-membrane deformable mirror for aberration compensation. *Applied Optics*, 38, 168-176.

## **INITIAL DISTRIBUTION LIST**

1. Defense Technical Information Center  
Ft. Belvoir, Virginia
2. Dudley Knox Library  
Naval Postgraduate School  
Monterey, California
3. Dr. Brij Agrawal  
Naval Postgraduate School  
Monterey, California
4. Dr. Jae-Jun Kim  
Naval Postgraduate School  
Monterey, California
5. Michael Doherty  
Naval Postgraduate School  
Monterey, California
6. Major Dan Burtz  
Naval Postgraduate School  
Monterey, California